1	Factors Affecting the Weakening Rate of Tropical Cyclones over
2	the Western North Pacific
3	Rong Fei ^{1,2,3} , Jing Xu ¹ , Yuqing Wang ^{3,1} , and Chi Yang ⁴
4	
5 6	¹ State Key Laboratory of Severe Weather, Chinese Academy of Meteorological Sciences, China Meteorological Administration, Beijing 100081, China
7 8	² College of Earth and Planetary Sciences, University of Chinese Academy of Sciences, Beijing, China
9 10	³ International Pacific Research Center and Department of Atmospheric Sciences, University of Hawaii at Manoa, Honolulu, HI 96822
l1 l2	⁴ College of Global Change and Earth System Science, Beijing Normal University, Beijing 100875, China
13 14 15	October 26, 2019 (submitted) February 6, 2020 (first revision) May 12, 2020 (second revision)
16	June 18, 2020 (final revision)
17	Dateline

Submitted to Monthly Weather Review

20 Corresponding author: Dr. Jing Xu, xujing@cma.gov.cn

21

18

19

22 Abstract

23

24

25

26

27

28

29

30

31

32

33

34

35

36

37

In this study, based on the 6-hourly tropical cyclone (TC) best-track data and the ERA-Interim reanalysis data, statistical analyses as well as a machine learning approach, XGBoost, are used to identify and quantify factors that affect the over-water weakening rate (WR) of TCs over the western North Pacific (WNP) during 1980-2017. Statistical analyses show that the TC rapid weakening events usually occur when intense TCs cross regions with sharp decrease in sea surface temperature (DSST) with relatively faster eastward or northward translational speeds, and move into regions with large environmental vertical wind shear (VWS) and dry conditions in the upshearleft quadrant. Results from XGBoost indicate that the relative intensity of TC (TC intensity normalized by its maximum potential intensity), DSST, and VWS are dominant factors determining TC WR, contributing 26.0%, 18.3% and 14.9% to TC WR, and 9, 5 and 5 m s⁻¹ day⁻¹ to the variability of TC WR, respectively. Relative humidity in the upshear-left quadrant of VWS, zonal translational speed, divergence at 200 hPa and meridional translational speed contribute 12.1%, 11.8%, 8.8% and 8.1% to TC WR, respectively, but only contribute 2–3 m s⁻¹ day⁻¹ to the variability of TC WR individually. These findings suggest that the improved accurate analysis and prediction of the dominant factors may lead to substantial improvements in the prediction of TC WR.

1. Introduction

38

39

40

41

42

43

44

45

46

47

48

49

50

51

52

53

54

55

56

57

Intensity prediction of tropical cyclones (TCs) is known to be challenging in operational TC forecasts (e.g., Elsberry et al. 2007; Kaplan et al. 2010). In the last decade or so, many efforts have been devoted to understanding crucial issues in the predictability of intensifying TC events, such as the rapid intensification (Tao et al. 2017; Jiang et al. 2018; Knaff et al. 2018) and the intensity change associated with evewall replacement cycles in TCs (Kossin and Sitkowski 2012; Kossin 2015; Kossin and DeMaria 2016). However, less studies have focused on the weakening process of TCs in the literature. TC weakening, especially rapid weakening (RW), is one of the major sources of large intensity forecasting errors. RW is often defined as a decrease of 30 kt (15.4 m s⁻¹ 1) or more in sustained near surface wind speed in 24 hours when the TC is over open water (Wood and Ritchie 2015). Statistical analyses show that the positive errors in official intensity forecast are often related to the TC-weakening cases, that is, their intensities are often overpredicted in official forecasts, especially for RW events (Wood and Ritchie 2015; Na et al. 2018). The overpredicted intensity forecast during the TC weakening stage may lead to overestimation of TC destructive potential and false alarm. Therefore, understanding of TC weakening processes is of great importance to improve TC intensity forecasting and destructive potential estimation.

TCs often form over warm tropical oceans with sea surface temperature (SST) over 26.5°C under favorable environmental atmospheric conditions, such as weak environmental vertical wind shear (VWS) and a moist mid-troposphere (Gray 1968). After their formation, TCs generally intensify and move away from the deep tropics. Some oceanic and atmospheric environmental

conditions may become unfavorable for a TC to intensify or even maintain its intensity, and thus the TC may experience its weakening phase. Among those conditions, SST is the most important factor influencing TC intensity change because it largely determines the energy supply to a TC through surface enthalpy flux from the underlying ocean. SST also is one of the key parameters that determine the maximum potential intensity (MPI) of a TC (Miller 1958; Emanuel 1986, 1988, 1995, and 1997; Holland 1997). In addition to SST, environmental atmospheric conditions may largely modulate the TC intensity, such as VWS in the environmental flow (e.g., DeMaria and Kaplan 1999; Zeng et al. 2007, 2008, 2010; Wang et al. 2015; Bukunt and Barnes 2015) and dry air in the near-core TC environment (Hendricks et al. 2010; Davis and Ahijevych 2012; Fowler and Galarneau 2017; Juračić and Raymond 2016). Strong VWS can lead to the weakening of a TC through ventilating the warm core, diluting moist air in the eyewall, and inducing large asymmetries in the inner core (Gray 1968; Frank and Ritchie 2001; Tang and Emanuel 2010, 2012; Riemer et al. 2010, 2013; Xu and Wang 2013; Fu and Wang 2017). Dry air in the near-core TC environment can lead to TC weakening if the dry air is entrained into the eyewall updraft to promote strong downdrafts, especially when large VWS exists (Davis and Ahijevych 2012; Fowler and Galarneau 2017). Moreover, some internal processes may also lead to TC intensity change, such as the development of strong outer spiral rainbands (Wang 2009) or the formation of a secondary eyewall and the related eyewall replacement cycle (Willoughby et al. 1982; Houze et al. 2007; Sikowski et al. 2011; Kossin and Sitkowski 2012; Yang et al. 2013; Kossin 2015; Kossin and DeMaria 2016).

58

59

60

61

62

63

64

65

66

67

68

69

70

71

72

73

74

75

76

77

78

As a small-probability event of TC weakening, TC RW is often defined as the bottom 5% of

all TC intensity change rates (e.g., Wood and Ritchie 2015; Ma et al. 2019). Wood and Ritchie (2015) showed that TC RW always occurred when a TC crossed a sharp SST gradient, encountered strong VWS, or experienced dry air intrusion over the North Atlantic and the eastern North Pacific. They found that these inhibiting environmental factors contribute either individually or jointly to TC RW; decreasing SST and increasing VWS contribute the most over the North Atlantic, while decreasing SST and low low-level relative humidity contribute the most in the eastern North Pacific. More recently, Ma et al. (2019) drew some similar conclusions on the dominating effect of VWS and sharp SST gradient on TC RW over the western North Pacific (WNP). However, they found that the effect of mid-level dry-air intrusion was insignificant during RW over the WNP compared with that in the North Atlantic and eastern North Pacific. They proposed that this may be due to the lack of prevailing mid-level dry-air layer (such as the Saharan air layer over the North Atlantic) over the WNP. The monsoon gyres are another special environmental factor that can induce TC RW over the tropical WNP. Liang et al. (2018) found that more than 40% of RW events south of 25°N were associated with the monsoon gyres. They suggested the monsoon gyres affect TC RW by modulating the TC structure.

79

80

81

82

83

84

85

86

87

88

89

90

91

92

93

94

95

96

97

98

99

Most previous studies have focused on individual factors influencing TC weakening or some weakening cases, or on composite analyses of environmental factors in classified TC intensity changes (such as RW and non RW) qualitatively. A systematic analysis of TC weakening rate (WR) as a continuous response and its relationship with the associated environmental factors over the WNP has not been conducted yet. The main objectives of this study are 1) to present the climatological characteristics of all over-water TC weakening cases, especially RW cases, over the

WNP, 2) to identify the dominant environmental factors that affect TC WR, and 3) to quantify the relative contributions of environmental factors to TC WR through sensitivity analysis based on a machine learning approach, the XGBoost method. The rest of this paper is organized as follows. Section 2 describes the data and methods used in this study. The basic climatological characteristics of TC weakening and RW are given in Section 3. The environmental factors that significantly affect TC WR are identified in section 4. The relative importance of various environmental factors to TC WR is analyzed and discussed in section 5. The main findings are summarized in the last section.

2. Data and methods

a. Data

100

101

102

103

104

105

106

107

108

109

110

111

112

113

114

115

116

117

118

119

Persistence and environmental variables used in this study are listed in Table 1. The Joint Typhoon Warning Center (JTWC) best-track dataset for WNP TCs during 1980–2017 was obtained from the IBTrACS version 4 (Knapp et al. 2010, 2018). The period since 1980 is generally considered the modern era, because geostationary satellite coverage has been nearly global and polar orbiting satellite data has been more widely available than previous years. Uncertainties in TC intensity and position estimations have been largely reduced since then (https://www.ncdc.noaa.gov/ibtracs/pdf/IBTrACS version4 Technical Details.pdf). The dataset includes 6-hourly TC location and maximum 1-min mean sustained surface wind speed. Only storms with tropical nature are included in our analysis. More than 95% of their 50-kt wind radii are less than 200 km. Since the TC inner-core can be fully covered by the 50-kt wind radius, TC cases with the storm center within 200 km from any landmass were excluded to avoid intensity change caused by significant topographic (including land) effects. Due to the contribution of a storm's translational speed (SPD) to the maximum wind speed of the storm, the initial maximum wind speeds in the best-track data cannot represent the purely circular component of maximum wind speeds. Therefore, to minimize the influence of storm translation on storm intensity, we subtracted 40% of the storm translational speed from the initial maximum wind speed for all TC cases and used the result as the measure of TC intensity (Vmax), as done by Emanuel et al. (2004). The TC intensity changes at 24-hour intervals were calculated accordingly. Cases with intensity change in 24 hours less than zero were defined as weakening cases. Only TCs with their centers south of 40°N while experiencing their weakening stages were considered in our analysis. In addition, to avoid the effect of short-term fluctuations in TC intensity, following Wood and Ritchie (2015), weakening cases with any 6-hourly intensification within a 24-hour window were also excluded.

As in Wood and Ritchie (2015), a 30 kt (15.4 m s⁻¹) decrease in Vmax in 24 hours was chosen as the threshold to define an RW case in this study. We used the magnitude of decrease in Vmax in 24 hours to quantify the WR (without a negative sign). Accordingly, slow weakening (SW) cases were defined as weakening cases with WR less than the RW threshold. In addition, TCs that experienced RW were simply called RW TCs and those non-RW TCs were called SW TCs. A total of 475 TCs with 3108 weakening cases, among which there were 153 RW TCs with 434 RW cases, were included in our following analyses.

The 6-hourly environmental data, including horizontal winds, relative humidity (RH) and SST, was derived from the European Centre for Medium-Range Weather Forecasts (ECMWF)

interim reanalysis (ERA-Interim), with a horizontal resolution of 0.75°×0.75° and at 37 pressure levels (Dee et al. 2011). The wind fields were filtered beforehand to remove all disturbances, including TCs, with wavelengths less than 1000 km based on the algorithm described in Kurihara et al. (1993). Specifically, the filtering algorithm is a local three-point smoothing operator applied iteratively in both the zonal and meridional directions. The TC environmental zonal wind (U) and meridional wind (V) were defined as the average over an annulus between radii of 200 and 800 km from the TC center, and VWS between 200 and 850 hPa were then calculated accordingly using the averaged environmental U and V. Note that this deep layer shear is a good indicator of environmental VWS effect on TCs and is widely used in the study of TC intensity change (e.g., Zeng et al. 2010; Wang et al. 2015). Large-scale divergence at 200 hPa (DIV200) was defined as the average of divergence in a radius of 1000 km from the TC center. The SST of each TC case was defined as the average in a radius of 300 km from the TC center. The above calculations all followed those used in SHIPS model (DeMaria and Kaplan 1999). The TC MPI was estimated using the algorithm described in Bister and Emanuel (2002).

b. The XGBoost methods

141

142

143

144

145

146

147

148

149

150

151

152

153

154

155

156

157

158

159

160

An effective machine learning method called Extreme Gradient Boosting (XGBoost) (Chen and Guestrin 2016) was used to quantitatively evaluate the relative contributions of environmental factors to TC WR. XGBoost is an implementation of gradient tree boosting (GTB) (Friedman 2001), one ensemble learning technique that has been used in many applications. Tree-based methods partition the feature space into a set of rectangles (leaves) through recursive binary splitting, and

then fit a simple model (e.g., a constant mean) in each one (Breiman et al. 1984). The feature space partition is fully described by a single tree (also known as classification and regression tree, or CART). Essentially, a tree is a piecewise constant or linear regression model. For a given dataset \mathcal{D} with n cases and m features, $\mathcal{D} = \{(\mathbf{x}_i, y_i)\}\ (\mathbf{x}_i \in \mathbb{R}^m, y_i \in \mathbb{R}, i = 1, \dots, n)$, a tree ensemble model uses K additive functions (trees) to predict the output,

$$\hat{y}_i = \phi(\mathbf{x}_i) = \sum_{k=1}^K f_k(\mathbf{x}_i), \ f_k \in \mathcal{F}, \tag{1}$$

where $\mathcal{F} = \{f(\mathbf{x}) = w_{q(\mathbf{x})}\}$ $(q: \mathbb{R}^m \to T, w \in \mathbb{R}^T)$ is the space of regression trees, q represents the structure of each tree that maps a case to the corresponding leaf index, T is the number of leaves in the tree, each f_k corresponds to an independent tree structure q and leaf weights w. Typically, additive models with a form as in Eq. (1) are fitted by minimizing a loss function averaged over the training data, such as the squared-error or a likelihood-based loss function. However, for the tree ensemble model, it is difficult to train using traditional numerical optimization techniques. Instead, the model can be trained in an additive manner, known as GTB. The number of additive trees K increases iteratively to make the value of loss function smaller and smaller. For a comprehensive introduction to CART and boosting methods, please refer to Hastie et al. (2009) Chapters 9 and 10.

XGBoost trains the set of functions used in Eq. (1) by minimizing the following regularized objective using GTB,

179
$$\mathcal{L}(\phi) = \sum_{i=1}^{n} l(\hat{y}_i, y_i) + \sum_{k=1}^{K} \Omega(f_k),$$
 (2)

where *l* is a differentiable convex loss function that measures the difference between the prediction

 $\hat{y_i}$ and the target y_i ; $\Omega(f_k) = \gamma T + \frac{1}{2}\lambda \sum_{j=1}^T w_j^2$, λ and γ are the regularization parameters. The second term Ω penalizes the complexity of the model. The additional regularization term helps to smooth the final learned weights to avoid over-fitting. As a result, while achieving high accuracy in representing the training cases, XGBoost exhibits great generalization ability to predict new cases. In addition, XGBoost provides a natural measure of feature importance. Importance is a relative score that indicates the fractional contribution of each feature to the model performance measure, and is 100% when summed over all features. Denote $g_i = \partial_{\hat{y}^{(t-1)}} l(y_i, \hat{y}^{(t-1)})$ and $h_i = \partial_{\hat{y}^{(t-1)}} l(y_i, \hat{y}^{(t-1)})$ for the *i*-th case at the *t*-th iteration in boosting the minimization of Eq. (2). For the split on a feature, assume that I_L and I_R are the case sets of the left and right nodes after the split. It can be shown that the approximate loss reduction, or the 'gain', after the split is given by

191
$$\operatorname{Gain} = \frac{1}{2} \left[\frac{G_L^2}{H_L + \lambda} + \frac{G_R^2}{H_R + \lambda} - \frac{(G_L + G_R)^2}{H_L + H_R + \lambda} \right] - \gamma, \tag{3}$$

where $G_L = \sum_{i \in I_L} g_i$, $G_R = \sum_{i \in I_R} g_i$, $H_L = \sum_{i \in I_L} h_i$ and $H_R = \sum_{i \in I_R} h_i$. Feature importance is calculated by first summing the gain of this feature's splits within a single tree, weighted by the number of related observations, and then averaged across all of the trees within the model. Once the model is fitted, importance is also evaluated accordingly for each feature. Even for a case where there are highly correlated features, XGBoost can also provide reliable estimates of importance for at least one of them, unlike in the multivariate linear models where their statistical significance could be "diluted" such that none of them would pass the significance test (Chen and Guestrin 2016).

Because of the above advantages, XGBoost has been successfully applied to investigate the nonlinear relationships between the response and features of a complex system. The fitted model

itself is much like a proxy model that encodes such relationships. To reveal a relationship of interest, visualization methods, such as Partial Dependence Plot (PDP) (Friedman, 2001) and Individual Conditional Expectation (ICE) plots (Goldstein et al. 2015), are usually applied. In practice, ICE is a series of model-predicted response curves, generated by varying the feature of interest over its value range while keeping the others fixed as observed for each training case. PDP is just the average curve of ICE curves over all cases. Other statistics of ICE, such as the quartiles, can also be plotted to reveal the variability of the response at the given value of the feature of interest. Take VWS as the example feature of interest. For each RW case, we can use the fitted model to predict TC WR for each of finely discretized values over the observed VWS range in turn, with all the other features fixed as observed. The ICE curve for each case is then achieved by linking the predicted values. If the feature of interest is almost independent of the other features, then its ICE curves as well as its PDP and quartile curves are approximately parallel (the interquartile range does not change with the feature). Otherwise, ICE curves may cross and their interquartile range may change with the feature, implying that the feature interacts with some of or all the others. It should be noted that for regression problems as we will deal with in section 5, each tree in the XGBoost model comprises of local linear regressions for individual leaves on the tree. Therefore, the ICE curves are zigzagged in nature. Since linear regressions are sensitive to outlier data, leaves containing outlier data might contribute to remarkable jumps on the predicted curves, as we will see in section 5b.

202

203

204

205

206

207

208

209

210

211

212

213

214

215

216

217

218

219

220

221

222

In this study, we use the XGBoost method to establish an empirical model of TC WR using all identified dominant environmental factors. It should be mentioned that, unlike SHIPS or other

related models, here the fitted model is not used for forecasting. Instead, it serves as an analysis tool to investigate the nonlinear relationships between TC WR and various factors. The relative importance of these factors is evaluated accordingly. Sensitivity and variability of TC WR in response to these individual factors are investigated using the ICE method based on the fitted model.

3. Characteristics of TC weakening over the WNP

223

224

225

226

227

228

229

230

231

232

233

234

235

236

237

238

239

240

241

242

Figure 1a shows the spatial distribution of TC WR and the frequency of weakening cases in each 2.5°×2.5° grid box in typhoon seasons (from June to November) during 1980–2017 over the WNP. It shows that most of the over-water weakening cases are located in the region of 15°-35°N, 125°-160°E and centered near 22°N, 130°E. Higher WR usually occurs north of 20°N. This is because TCs often experience their major weakening phase at latitudes north of 20°N after their intensification stages. Moreover, unfavorable environmental conditions at mid-latitudes may enhance the WR of TCs. Note that there is a local maximum in WR just off the coast of Japan, which is due to the relatively high WR of only one case falling in that grid box. Figures 1b and 1c show RW TC and SW TC tracks, respectively. The SW stages during RW TC lifetimes are indicated as grey, while the RW stages are highlighted as black. The RW stages usually start at the recurving points of TC tracks northward or northeastward, which is probably related to the sharp decrease in SST along the TC tracks or/and the change in environmental wind field. This is consistent with the results of Ma et al. (2019), who also found that the RW cases usually occur as TCs crossed a sharp SST gradient over the WNP.

Note that few RW TCs were observed in the South China Sea (SCS) in our analysis. This is

mainly due to relatively few strong TCs over the SCS, and the warm SST greater than 28°C in SCS is also unfavorable for TC weakening (Figs. 1b and 1c). Only TCs that formed in the SCS were counted, while those that entered the SCS after landfall but formed outside the SCS were not included in our analysis. Note also that some RW TCs occurred in the tropical WNP, which should be related to monsoon gyres as recently studied by Liang et al. (2018). They found that although less than one-third of RW events occurred south of 25°N, more than 40% of them were associated with monsoon gyres over the WNP. They showed that about 85% of these RW events were usually observed near the center of a monsoon gyre when a TC made a sudden northward turn. Comparing Figs. 1b and 1c, we can see that there are no distinct differences in geographical distribution between the RW and SW TC tracks, particularly in the high WR regions north of 25°N, although the initial stages of SW TCs were farther southward than those of RW TCs. This suggests that the two groups of TCs were governed by other factors, such as persistence and/or environmental factors. Figure 2 displays the monthly distributions of the numbers of total weakening TCs and RW TCs (Fig. 2a), and the numbers of total weakening cases and RW cases (Fig. 2b), as well as their respective ratios. Here a weakening case refers to a 6-hourly observation of a TC with a decrease in Vmax in 24 hours, while a RW case is a weakening case with a decrease of at least 15.4 m s⁻¹ in Vmax in 24 hours. It can be seen that the numbers of both RW TCs and RW cases increase from June to October, with 31 RW TCs out of total 87 TCs (36%) and 82 RW cases out of 555 weakening cases (15%), respectively, in October. However, the ratio of RW TCs to all TCs and that of RW cases to all weakening cases increase significantly from 14% (15 out of 110 TCs) and 5% (33 out of 675 weakening cases) in August to 49% (19 out of 39 TCs) and 25% (62 out of 250 weakening

243

244

245

246

247

248

249

250

251

252

253

254

255

256

257

258

259

260

261

262

263

cases) in November. In general, TC RW occurs more frequently in fall than in summer over the WNP, which is likely to be associated with the lower MPI resulting from the lower SST in fall than in summer (Ge et al. 2017), and with atmospheric variations as well, such as drier mid-troposphere and stronger vertical wind shear in fall than in summer.

264

265

266

267

268

269

270

271

272

273

274

275

276

277

278

279

280

281

282

283

284

Table 2 compares the statistics of SW and RW TCs as a function of the weakening duration. Here we define the weakening duration as a period of ongoing weakening without any intensification of each TC, calculated as a continuous and overlapping 24-hour weakening period. It is different from a weakening case, which refers to the weakening over a 24-hour period. The average weakening duration (including both SW and RW TCs) is 67 hours per TC. The frequency of weakening TCs decreases with increasing weakening duration. TCs with their weakening duration more than 6 days account for only 6.2% of total TCs. Comparing the weakening duration of RW and SW TCs, we can find that TCs experiencing RW periods usually have slightly longer weakening duration than those only experiencing SW in their lifetimes. The average weakening duration of RW TCs is 82 hours, while that of SW TCs is only 62 hours. Totally, 434 RW cases from 153 RW TCs occurred in the WNP. This means that on average each RW TC produces about 3 overlapping RW cases, or equivalently, each RW TC experiences the RW period of about 36 hours since the TC best-track records used in the analysis are 6-hourly. This is comparable with the 36 and 30 hours of average RW durations in the eastern North Pacific and North Atlantic, respectively, reported in Wood and Ritchie (2015).

TCs that experienced long RW durations usually have a relatively high lifetime maximum intensity (LMI). As we can see from Table 2, RW TCs with weakening duration longer than 48

hours have an average LMI over 56 m s⁻¹, while the averaged LMI of SW TCs with weakening duration longer than 48 hours is only 36 m s⁻¹. Note that three TCs weakened for more than 192 hours (8 days): KIM (1986), ELE (2002) and IOKE (2006). KIM and IOKE experienced RW periods after they reached their LMIs of 67.8 m s⁻¹ and 70.4 m s⁻¹, respectively. ELE experienced its relatively high maximum WR of 13.4 m s⁻¹ day⁻¹ after peaking its LMI of 57.5 m s⁻¹. Further analysis indicates that the weakening phases of about 34% RW TCs (52 out of 153) lasted for longer than 96 hours in the WNP. For RW TCs with weakening duration shorter than 60 hours, the RW periods are mostly (85.8%) consecutive, while for the others whose weakening duration was longer than 60 hours among RW TCs, most (73.3%) of them are discontinuous. Moreover, there are 86.1% (409 out of 475) of TCs undergoing their first weakening phase, and about 29.4% (45 out of 153) of RW TCs undergoing their first RW period within 24 hours after they reached their LMIs. This indicates that only a minority of TCs in the WNP could maintain very high intensities after their LMIs for an appreciable period. This is probably because when a TC developed to a high intensity, it had already moved to a less favorable environment than before, such as cooler SST, stronger vertical wind shear and drier mid-troposphere. The detailed roles of the environmental factors will be further examined in the next section.

4. Factors affecting TC weakening rate

285

286

287

288

289

290

291

292

293

294

295

296

297

298

299

300

301

302

303

304

Weakening is often the last stage of a TC and mostly occurs when the storm moves out of the deep tropics and enters a less favorable environment. In this section, we discuss factors affecting the TC over-water WR, including both the TC persistence variables and large-scale environmental

variables (Table 3).

305

306

307

308

309

310

311

312

313

314

315

316

317

318

319

320

321

322

323

324

a. Persistence factors and SST

Figure 3 shows the scatter diagrams of the 24-hour WR against Vmax, SST, relative intensity (defined as the ratio of the current TC intensity to its theoretical MPI, namely Vmax/MPI, hereafter POT), 24-hour SST change along TC track (DSST), zonal and meridional translational speeds (USPD and VSPD) of all weakening TC cases, together with their corresponding fitted 50th, 75th and 95th percentiles of WRs. All the fitted percentiles of TC WRs increase with increasing Vmax (Fig. 3a), showing an approximately linear dependence of TC WR on Vmax. Very few RW cases occur for storms with intensity less than 35 m s⁻¹ because tropical storms (TS) are too weak to reach the RW threshold of 15.4 m s⁻¹ day⁻¹. The significant linear correlation between TC WR and Vmax (r = 0.37) (Table 3) indicates that Vmax is an important factor determining the subsequent WR. Namely, a TC with a greater intensity at and after it reaches its LMI tends to have a greater WR. This could be due to the fact that an intense TC typically experiences a relatively long intensification stage, often moves out of deep tropics (Fig. 1), and is about to enter regions with decreasing SST or environmental atmospheric conditions unfavorable for TCs to maintain high intensity. The underlying SST largely determines the surface enthalpy flux in the inner core of a TC and thus is a key factor affecting TC intensity change. As we can see from Fig. 3b, TC WR is negatively correlated with SST (r = -0.16) (Table 3). In particular, the fitted 95th percentile shows an obvious decreasing trend of the upper bound of TC WR with increasing SST, confirming that SST is an important factor contributing to TC WR. Note that large TC WR higher than 30 m s⁻¹ day⁻¹ occurs over SST between 26.5°C and 28.5°C rather than the coldest SST (Fig. 3b). This is because TCs at relatively low SSTs are often already weak so that their WRs could not be too large.

325

326

327

328

329

330

331

332

333

334

335

336

337

338

339

340

341

342

343

344

345

Since current Vmax and SST are both important for the subsequent WR, and SST is a key parameter determining the TC MPI, we further examine the relationship between TC WR and POT (Fig. 3c). POT represents how far the current TC intensity is from its MPI. Similar to Vmax, POT is also positively correlated with TC WR (r = 0.4) (Table 3). This implies that TCs with their intensities closer to MPI may weaken more rapidly. The greater POT indicates either stronger intensity or lower MPI, or both, which provides relatively greater potential for a TC to weaken. Particularly, greater POT implies that the real upper limit of intensity will drop below the current intensity more easily and considerably when a TC encounters detrimental environmental conditions, such as strong vertical wind shear and dry middle troposphere. Note that there are about 12.9% of the weakening cases with POT greater than 1.0, implying that some TCs are superintense (Persing and Montgomery 2003). This is not unusual because observations did show that real TCs could have intensity higher than their corresponding theoretical MPIs (e.g., Montgomery et al. 2006). This could also happen when a TC moves quickly to pass over cold water (because of limited time for the storm to adjust to its environment; Emanuel 2000).

The change in SST along the subsequent TC track could be a better indication of the energy input from the underlying ocean to the TC than SST under the current TC location. Therefore, it is expected that the TC WR would be correlated with the decrease in SST more closely than with the SST itself. This is indeed the case as we can see in Fig. 3d, which shows the relationship between

the subsequent DSST along the TC track and the subsequent 24-hour TC WR. All the fitted percentiles show that TC WR increases with the decrease in SST (namely negative DSST). The negative correlation of TC WR with DSST (r = -0.26) is higher than that with SST (Table 3), suggesting that the greater decrease in SST can result in higher TC WR. This is consistent with the fact that most RW cases occurred for TCs crossing a sharp SST gradient in the WNP (Fig. 1b). The SPD of a TC is also considered a factor affecting TC intensity change (Zeng et al. 2007, 2008). Previous studies have shown that too low SPD is unfavorable for rapid intensification because of the negative feedback from the cooling SST induced by upwelling (e.g., Walker et al. 2014). However, a fast movement is unfavorable for TC intensification likely due in part to the generation of large asymmetries in the TC inner-core structure (Peng et al. 1999; Zeng et al. 2007, 2008). As a result, we can consider that fast movement may favor TC RW, that is, WR may increase with increasing SPD. This tendency is clear in both Figs. 3e and 3f, which show the relationships between TC WR and its fitted quantiles against USPD and VSPD, respectively. Both USPD and VSPD are positively correlated with TC WR, with their correlation coefficients being 0.29 and 0.26, respectively (Table 3). This means that the TC WR becomes higher when a TC moves eastward and/or northward. This is also consistent with the fact that most RW TCs occur after they recurve northward and northeastward and enter the mid-latitude westerlies as shown in Fig. 1b. Note that the RW TCs also occur in the region where SST decreases rapidly along the TC tracks, as we can see in Fig. 1b. Therefore, contributions to the positive correlation of TC WR and SPD are not only from the fast translation itself, but also from other related changes in SST and atmospheric

346

347

348

349

350

351

352

353

354

355

356

357

358

359

360

361

362

363

364

365

366

environment, such as VWS, as we will discuss further in section 5.

Figure 4 compares the frequency and cumulative percentage distributions of SW and RW cases against several factors discussed above. The RW cases mostly occur in TCs with Vmax between 40 m s⁻¹ and 65 m s⁻¹, accounting for 71.4% of RW cases; whereas 90.8% of SW cases are evenly distributed in TCs with Vmax lower than 65 m s⁻¹ (Fig. 4a). The cumulative percentage distributions show that 80% and 50% of RW cases occur with Vmax higher than 42 m s⁻¹ and 52 m s⁻¹, respectively, while those of SW cases occur with Vmax higher than 24 m s⁻¹ and 40 m s⁻¹, respectively. The RW cases tend to occur at colder SST than the SW cases do, with the highest frequency of RW and SW cases occurring at 27.5°C and 28.5°C, respectively (Fig. 4b). The majority (82.3%) of RW cases occur when POT is greater than 0.7, with their highest frequency occurring when POT is between 0.8 and 1.0, and few RW cases occur with POT less than 0.4 (Fig. 4c). Compared with RW cases, SW cases are more evenly distributed over POT between 0.2 and 1.0. This further confirms that the intense TCs with their intensities close to their upper limits are subject to greater potential for RW. The difference in frequency distribution between SW and RW cases is obvious with respect to DSST (Fig. 4d). A large amount (57.0%) of RW cases occur in regions with DSST less than -1°C day⁻¹, while the majority (77.5%) of SW cases occur in DSST greater than -1°C day⁻¹. The average DSST for the SW and RW cases is -0.81°C and -1.76°C day⁻¹ ¹, respectively. The latter is slightly stronger than the average DSST for the onset of RW in the eastern North Pacific (-1.0°C) and the North Atlantic (-1.5°C), respectively (Wood and Ritchie 2015).

367

368

369

370

371

372

373

374

375

376

377

378

379

380

381

382

383

384

385

386

387

In addition, most RW cases have SPD between 4 and 8 m s $^{-1}$, while most SW cases have SPD between 2 and 6 m s $^{-1}$ (Fig. 4e). About 53.5% of RW cases but only 24.6% of SW cases occur when

SPD is higher than 6 m s⁻¹. The higher SPD of RW cases results from both the higher USPD and VSPD (Figs. 4e and 4f). Note that although USPD can be either westward or eastward for both RW and SW cases, VSPD is mostly northward and is higher for RW than for SW (Fig. 4f). The stronger northward component of motion for RW implies that the TC was moving into higher latitudes often with decreasing SST, which is consistent with the results shown in Figs. 3e and 3f.

b. Environmental atmospheric factors

We first examine the vertical profiles of the composite U and V over the TCs for SW and RW cases, respectively, conditional on TC POT (Fig. 5). POT represents the potential of TC weakening, as discussed above. On average, the SW group is embedded in zonal wind with easterly flow about 1–2 m s⁻¹ below 850 hPa and westerly flow above, up to higher than 5 m s⁻¹ in the upper troposphere (Fig. 5a), and uniform southerly wind about 1–2 m s⁻¹ throughout the troposphere (Fig. 5d). In contrast, both U and V are much higher in the RW group, with the maximum U and V higher than 9 m s⁻¹ (Fig. 5b) and 4 m s⁻¹ (Fig. 5e), respectively, in the upper troposphere. The stronger westerly in the upper troposphere and easterly below 800 hPa imply stronger deep-layer westerly VWS in RW cases (Fig. 5b) than in SW cases (Fig. 5a). The stronger southerly wind in the upper troposphere also implies stronger deep-layer VWS in RW cases (Fig. 5d) than in SW cases (Fig. 5e). Note that the relatively stronger northerly appears for POT less than 0.65 in the RW group below 900 hPa, referring to TCs with moderate POT that encounter the mid-latitude westerly after their LMI.

The differences in vertical wind profiles between the RW and SW groups can be more clearly seen from Figs. 5c and 5f. Large differences in both the westerly and southerly flow of the RW and

SW groups are present in the upper troposphere, while the difference in the lower troposphere is as small as 1.0–1.5 m s⁻¹, especially for moderate POT. This implies stronger VWS in the upper troposphere in RW cases. Previous studies have also shown that the upper-level VWS can ventilate the warm core of a TC more efficiently (Gray 1968; Fu et al. 2019). The upper-level VWS can also act to shrink the vertical extent of the axisymmetric vortex, reducing the warm core and leading to TC weakening (Knaff et al. 2004). In addition, the slightly stronger lower- to middle-level VWS tends to enhance both the ventilation of the mid-level vortex with dry environmental air and the flushing of low-entropy air into the frictional inflow layer (Tang and Emanuel 2010; Riemer et al. 2010, 2013).

To estimate the extent to which VWS affects TC WR, we show in Fig. 6a the scatter diagram of TC WR against the deep-layer VWS, which is evaluated as $\sqrt{(U_{200}-U_{850})^2+(V_{200}-V_{850})^2}$, where the subscripts "200" and "850" indicate environmental U or V at 200 and 850 hPa, respectively. In general, all the 50th, 75th and 95th percentiles of WR increase with increasing VWS. TC WR is positively correlated with VWS (r = 0.26) (Table 3), which is consistent with previous findings (Zeng et al. 2007; Wang et al. 2015). The frequency distribution of RW cases peaks at VWS about 10–12 m s⁻¹ while that of SW cases peaks at VWS about 6–8 m s⁻¹. The RW cases with VWS stronger than 10 m s⁻¹ account for 65.0% of all RW cases, whereas the percentage is only 36.5% for SW cases with VWS stronger than 10 m s⁻¹ (Fig. 6b).

Mid-level humidity is another factor that is often considered to affect TC intensity and intensity change. Most previous studies have mainly explored the influence of the azimuthal-mean RH (Kaplan and DeMaria 2003; Hendricks et al. 2010; Ma et al. 2019), while some studies show that

the azimuthally asymmetric RH is more important to TC intensity change (Shu and Wu 2009; Wu et al. 2012) than only the azimuthal-mean RH. Considering the close relationship between dry air intrusion and VWS (Tang and Emanuel 2010, 2012), we examined the correlations between TC WR and RHs averaged vertically over 300-850 hPa and horizontally over an annulus with 200and 800-km radii from the TC center in four quadrants with respect to the direction of VWS (namely, the downshear-left, downshear-right, upshear-left, and upshear-right quadrants; Table 1), respectively. Results show that the RH in the upshear-left quadrant (RHUL) has the highest negative correlation (r = -0.26) with TC WR among the four quadrants, while RHs in the other quadrants are not significantly correlated with TC WR (Table 3). We also calculated RH averaged over different layers (such as between 400 – 700 hPa and between 850 – 700 hPa) and found that the 300 – 850-hPa RH has the highest correlation with TC WR. That is to say, low RHUL has a significant negative effect on TC intensity and is likely favorable for TC weakening. This is probably because under the influence of VWS, mid-level environmental air is more likely to be transported into the TC eyewall from the upshear-left quadrant (Cram et al. 2007), lowering entropy in the eyewall and suppressing eyewall convection, thus leading to TC weakening. As we can see from Fig. 6c, which shows TC WR and various percentiles against RHUL, WR exhibits an overall decreasing trend with the increasing RHUL, which is more pronounced when RHUL is less than 40%. The frequency distributions of SW and RW cases against RHUL (Fig. 6d) indicate that RW cases occur more frequently with RHUL lower than 35% while SW cases occur more frequently with RHUL greater than 45%.

429

430

431

432

433

434

435

436

437

438

439

440

441

442

443

444

445

446

447

448

449

Large-scale divergence in the upper troposphere can also influence TC intensity change

(Hendricks et al. 2010). Therefore, we checked the relationship between TC WR and DIV200 with the results shown in Fig. 6e. It seems that TC WR is positively correlated with DIV200, but the correlation is statistically insignificant with r=0.07 only (Table 3). The frequency of RW cases peaks at DIV200 around $2.5\times10^{-6}~\rm s^{-1}$, and is generally greater than that in SW cases (Fig. 6f). This is consistent with the finding of Hendricks et al. (2010), who found that the composite upper-level divergence was the greatest in the composite of weakening TCs among all the TC intensity change groups (neutral, intensifying, rapid intensifying and weakening). However, this result contradicts previous studies by Kaplan et al. (2010) and Lee et al. (2015), who found that stronger upper-level divergence provides better chance for a TC to intensify. Hendricks et al. (2010) proposed that this is mainly because weakening TCs are often interacting with upper-level troughs and are on average more intense and have larger extent of the upper-level outflow than neutral and intensifying TCs. Therefore, DIV200 is still considered as a possible factor affecting TC WR in our analysis.

The above analyses demonstrate that 1) the TC WR is positively correlated with Vmax and POT, the latter can represent the potential of TC weakening; 2) TC WR is highly correlated with the storm SPD and SST gradient; and 3) the atmospheric factors, such as deep-layer VWS, RHUL, and DIV200, can also affect TC WR. Note that these factors are not necessarily independent since some factors may correlate with each other significantly. Such dependence needs to be considered if any linear regression model is to be developed. In the next section, however, we apply the XGBoost method described in section 2, to quantify the relative importance of individual factors to TC WR and to examine the sensitivity of TC WR to these factors, by making full use of its capability to capture nonlinear relationships but little affected by the dependence among different

471 factors.

472

473

474

475

476

477

478

479

480

481

482

483

484

485

486

487

488

489

490

5. Relative contributions of individual factors to TC WR

a. Model fitting and validation

The XGBoost model described in section 2 is used to quantify the relative importance of factors to TC WR, including TC persistent factors (POT, USPD and VSPD), DSST and environmental atmospheric factors (VWS, RHUL and DIV200) identified in section 4 (Table 3). These factors are used as input features to the XGBoost model for all weakening TC cases. With some typical parameter settings (learning rate $\eta = 0.3$, minimum loss reduction $\gamma = 0$ and the maximum depth of a tree = 7; refer to https://xgboost.readthedocs.io/en/latest/parameter.html for a detailed description), the root mean square error (RMSE) of the fitted TC WR stabilizes at 9.6× 10^{-4} m s⁻¹ day⁻¹ after about 600 iterations (therefore, the number of trees K = 600). This means that the XGBoost model with the identified input factors can well reproduce TC WR in the dataset. Note that the fitting error does not indicate the prediction error. To indicate the model's generalization (prediction) ability, a 100-fold cross validation (CV) of the same model was further carried out. The dataset was randomly divided into 100 subsamples with equal size (about 30 cases), each of which was used as testing data with all the others pooled together as training data in turn for once. The 100-fold mean RMSE of the prediction of testing data is 4.5 m s⁻¹ day⁻¹, which can be viewed as a measure of the model prediction performance. As a comparison, the fitting and CV RMSEs for a counterpart multiple linear model fitted to the same dataset are both around 5.0 m s⁻¹ day⁻¹. For predictive models, there is a ubiquitous trade-off between model bias and prediction

variance (uncertainty), and linear models have the property of high bias and low variance in general (Hastie et al 2009, Chapter 2).

The above comparison suggests that the very small RMSE of the fitted XGBoost model is due to its capability of modeling nonlinearity, rather than overfitting (otherwise the CV RMSE would have been much higher than that of the linear model). If used for prediction purpose, the CV RMSE could be reduced by tuning the model parameters, with a cost of increasing the fitting RMSE. In this work, however, the fitted model well captured the relationships between TC WR and the factors of interest so that it serves as a powerful tool for the analysis of relative importance of factors.

b. Feature importance and sensitivity analysis

Figure 7 shows the relative importance of the identified factors to TC WR, namely to what extent TC WR is contributed by each of the input factors, by using the method described in section 2. We can see that POT is the most important factor in controlling TC WR, which contributes 26.0% to TC WR. The rest are DSST (18.3%), VWS (14.9%), RHUL (12.1%), USPD (11.8%), DIV200 (8.8%), and VSPD (8.1%), respectively. This is broadly consistent with the descending order of the correlation coefficients shown in Table 3, except for USPD and VSPD, which could be due to their closely correlations with DSST and VWS.

In addition to the overall relative importance of individual factors, we also examined the sensitivity and variability of TC WR in response to the variation in each factor by conducting several sets of sensitivity experiments based on the ICE method (section 2). Firstly, we choose a target feature x_s (e.g., POT) to analyze, while keeping all other features \mathbf{x}_c for each case unchanged

as the background. By varying x_s within its value range for each individual case, a set of the model-predicted responses can be obtained as a function of x_s , conditional on the observed \mathbf{x}_c . Secondly, we plot all ICE curves for cases from each set of sensitivity experiments (thin curves in Figs. 8 and 9). Each curve reflects the predicted response to x_s conditional on the observed \mathbf{x}_c for each case. As we noted in section 2, these curves are zigzagged with a few remarkable jumps due to outlier data. Therefore, we finally fit four percentiles (25th, 50th, 75th, and 95th percentiles, thick curves) to all the curves, which are much more robust, to evaluate the variability of predicted response to each factor (a set of experiments).

Figure 8a shows the relationship between TC WR and POT for each weakening case in thin black curves and the corresponding 25th, 50th, 75th, and 95th percentiles of the WRs predicted by the model. The variability of the curves reveals the extent of WR's heterogeneity with POT changing within its valid observational range, which can be considered as the WRs of a weakening TC in a unique environment with different POTs. The predicted WR increases with increasing POT and shows an approximately linear dependence on POT. Note that the model also yields a few RW cases at POT below 0.5, consistent with observations shown in Fig. 3. In particular, the variation in the median of the predicted WR is about 9 m s⁻¹ day⁻¹ (from 4 to 13 m s⁻¹ day⁻¹) as POT varies from 0.25 to 1.2, while that in the 95th percentile is 13 m s⁻¹ (from 8 to 21 m s⁻¹ day⁻¹). This means that POT alone can induce a variability in WR by 9 m s⁻¹ day⁻¹ under the averaged environmental conditions, while under the extremely unfavorable conditions, such as strong VWS and/or sharp DSST, POT can cause a variability in WR by as much as 13 m s⁻¹ day⁻¹. The variability of WR, which is measured as the interquartile range between the 25th and 75th percentiles, increases with

increasing POT under the same environmental conditions. For example, the interquartile range increases from 3 m s⁻¹ dav⁻¹ at POT less than 0.4 to 6 m s⁻¹ dav⁻¹ at POT around 1.0 (Fig. 8a).

The TC WR shows a general decrease with increasing DSST along the TC track (Fig. 8b). The predicted WR decreases with increasing DSST for DSST larger than -2° C but changes less for DSST smaller than -2° C (Fig. 4d). The median of WR decreases by about 5 m s⁻¹ day⁻¹ (from 11 to 6 m s⁻¹ day⁻¹) and the extreme WR (the 95th percentile) decreases by 5 m s⁻¹ day⁻¹ (from 20 to 15 m s⁻¹ day⁻¹) as DSST increases from -2° C to 1°C, meanwhile the interquartile range of WR decreases from about 7 to 5 m s⁻¹ day⁻¹.

Consistent with previous studies, VWS is a major factor leading to TC weakening. It can induce a variation in the median of WR by about 5 m s⁻¹ day⁻¹ (from 7 to 12 m s⁻¹ day⁻¹) for VWS in the observational range of 0–16 m s⁻¹ (Fig. 8c), which is considerably smaller than that induced by POT, but is comparable with that induced by DSST. All predicted percentiles of WR increase with increasing VWS when VWS is stronger than 10 m s⁻¹. This agrees with previously reported threshold of about 10 m s⁻¹ above which VWS can have a significant detrimental effect on TC intensity and intensification (Zeng et al. 2007, 2008; Rios-Berrios and Torn 2017). Note that the fitted 95th percentile of WRs is more than 16 m s⁻¹ day⁻¹ for any VWS, implying that RW can even occur under weak VWS due to greater effects of other factors, such as large POT and negative DSST, as shown in Figs. 8a and 8b. This is consistent with the estimated relative importance of the contributing factors shown in Fig. 7.

Compared with the sensitivity to POT, DSST, and VWS, TC WR seems insensitive to the other environmental factors. Changes in TC WR against RHUL and DIV200 are shown in Figs. 8d

and 9b, respectively. The median of the predicted WR changes by about 2 m s⁻¹ day⁻¹ with either RHUL or DIV200. In addition, TC WR is also less sensitive to both USPD and VSPD and changes by only about 3 and 2 m s⁻¹ day⁻¹ within their respective ranges of USPD and VSPD, respectively (Figs. 9a and 9c). The above results demonstrate that POT, DSST and VWS are important factors that dominantly determine TC WR, and as a result, TC WR is sensitive to these factors. Other factors are of secondary importance to WR. Although the linear correlations between TC WR and other factors may also comparable with those between TC WR and the dominating factors, such as VWS, their effects are often not independent of the dominating factors. This partly explains why these factors are shown to be of secondary importance to TC WR. The application of XGBoost in this study shows that this model has advantages to avoid the feature inter-dependence issue and provides more accurate estimate of relative importance compared with the widely-used linear regression model, as well as to provide an approach to sensitivity analysis.

6. Conclusions and discussion

The over-water TC weakening is controlled by the underlying ocean, large-scale atmospheric environmental conditions, and internal dynamical processes. In this study, both the persistence and environmental factors that affect the WR of over-water TCs in the WNP are statistically analyzed and evaluated based on the IBTrACS TC best-track data and 6-hourly ERA-Interim reanalysis data during 1980–2017. A machine learning approach, XGBoost, is used to quantify the relative importance of these factors to TC WR. In the WNP, an over-water TC weakening event can last up to 216 hours (9 days) with an average weakening duration of 66.7 hours. On average, RW TCs tend

to have a weakening duration of about 82.0 hours, which is much longer than that of 61.5 hours for SW TCs. The average RW TC undergoes the RW period for 36 hours, which is comparable with the averaged 36 hours and 30 hours in the eastern North Pacific and North Atlantic. The proportion of RW TCs to all TCs shows a distinct seasonal variation, with the maximum in November and the minimum in August. This suggests that RW occurs more frequently in fall than in summer in the WNP, which could be due to the lower MPI resulting from the lower SST in fall than in summer.

Statistical analysis shows that five factors are found to be positively correlated with TC WR, i.e., Vmax, POT, VWS, USPD, and VSPD. Three other factors, including SST, DSST and RHUL, are found to be negatively correlated with TC WR. Second to POT, DSST, SPD, VWS and RHUL are also highly correlated with TC WR, while DIV200 is statistically insignificant. Consistent with the correlation analysis, a comparison between RW and SW cases indicates that RW cases often occur with higher Vmax or POT, in regions with lower SST and sharper SST gradient, and move farther eastward and/or northward than SW cases. RW cases often occur in stronger VWS and/or under greater upper-tropospheric divergence, and lower RHUL. A comparison of the environmental U and V profiles between SW and RW cases indicates that westerly wind in the upper troposphere and easterly wind below 800 hPa are stronger, corresponding to stronger westerly VWS, in RW cases.

Note that as for the effect of mid-level RH on TC weakening in the WNP, our results are not in full agreement with Ma et al. (2019). They found that the role of environmental mid-level humidity is statistically insignificant probably because of the lack of prevailing mid-level dry-air layer over the WNP. Our results show that the RH in the upshear-left quadrant has a significant

negative correlation with TC WR, while RHs in the other quadrants are not significantly correlated with TC WR, suggesting that the mid-level dry air is more likely to be transported into the TC eyewall from the upshear-left quadrant of VWS, and thus leading to TC weakening.

594

595

596

597

598

599

600

601

602

603

604

605

606

607

608

609

610

611

612

613

614

The XGBoost model, a well-applied basic machine learning algorithm, is adopted to quantify the relative importance of the above factors, and the ICE method is used to conduct sensitivity experiments to examine the variability of TC WR in response to the variation of each factor. Results from these analyses confirm that POT is the most important factor among all the identified factors and contributes 26.0% to TC WR. DSST, VWS, RHUL, USPD, DIV200 and VSPD contribute 18.3%, 14.9%, 12.1%, 11.8%, 8.9%, and 8.1%, respectively, to WR. These results are in good agreement with their ranks of linear correlations with TC WR, except that USPD and VSPD seem not as important to TC WR as shown in the correlation analysis. This is most likely because of their dependence on either DSST or VWS or both. The sensitivity experiments using the ICE method show that POT can produce variations of about 9 m s⁻¹ day⁻¹ in TC WR under average environmental conditions, with variations of up to 13 m s⁻¹ day⁻¹ under extremely unfavorable environmental conditions, such as strong VWS and sharp DSST. The dominant effect of POT on TC WR may be largely due to the fact that most TCs reach their LMIs when they are close to latitudes where mid-latitude westerly troughs, strong VWS, and sharp SST gradient often coexist. Compared with POT, both DSST and VWS are of the second importance to TC WR, contributing about 5 m s⁻¹ day⁻¹ to the variability of TC WR, and the other factors contribute only 2–3 m s⁻¹ day⁻¹ ¹ on average.

Results from this study demonstrate that TC WR is largely controlled by both the persistence

and preexisting oceanic and environmental atmospheric factors, among which POT, DSST, and VWS are the most important. Although other factors, such as RHUL and SPD, show significant linear correlations with TC WR, they are often not independent of either VWS or DSST or both. As a result, the variability of TC WR in response to changes in these factors is relatively small, suggesting that although the prediction of TC WR may be improved to some extent, little improvements can be achieved by improving the accuracy of those factors. In contrast, improved analysis and prediction of POT, DSST and VWS may lead to substantial improvements in the prediction of TC WR. Finally, it is unclear how effective the analysis approach adopted in this study would be if it is used to quantify TC intensification rate. Moreover, the use of XGBoost in forecasting the TC intensity over the WNP has recently been attempted (Jin et al. 2019), suggesting that it may also has potential use in the TC intensity forecasts. These will be other topics we plan to explore in our future work.

Acknowledgments: This study has been supported in part by the National Key R&D Program of China under grants 2017YFC1501602, the National Natural Science Foundation of China under grant 41875057, 41730960 and 41675044, and in part by the NSF grants AGS-1326524 and AGS-1834300. R. Fei is funded by China Scholarship Council (File 201905330037). The TC best-track data were downloaded from https://www.ncdc.noaa.gov/ibtracs/. The ERA-Interim data were downloaded from http://apps.ecmwf.int/datasets/. The authors would like to thank the anonymous reviewers for their valuable comments and suggestions.

References

635

- Bister, M., and K. A. Emanuel, 2002: Low frequency variability of tropical cyclone potential
- intensity. 1. Interannual to interdecadal variability. J. Geophys. Res., 107, 4801,
- 638 https://doi.org/10.1029/2001JD000776
- Breiman L., J. H. Friedman, C. J. Stone, and R. A. Olshen, 1984: Classification and Regression
- Trees. Chapman & Hall.
- Bukunt, B. P., and G. M. Barnes, 2015: The subtropical jet stream delivers the coup de grace to
- Hurricane Felicia (2009). Wea. Forecasting, 30, 1039-1049, https://doi.org/10.1175/WAF-D-
- 643 15-0004.1
- 644 Chen, T., and C. Guestrin, 2016: XGBoost: A scalable tree boosting system. Proc. 22nd ACM
- 645 SIGKDD Int. Conf. on Knowledge Discovery and Data Mining, 2016, San Francisco, CA,
- Association for Computing Machinery, 785–794, http://dx.doi.org/10.1145/2939672.2939785
- 647 Cram, T. A., J. Persing, M. T. Montgomery, and S. A. Braun, 2007: A Lagrangian trajectory view
- on transport and mixing processes between the eye, eyewall, and environment using a high-
- resolution simulation of Hurricane Bonnie (1998). J. Atmos. Sci., 64, 1835–1856,
- 650 https://doi.org/10.1175/JAS3921.1
- Davis, C. A., and D. A. Ahijevych, 2012: Mesoscale structural evolution of three tropical weather
- 652 systems observed during PREDICT. J. Atmos. Sci., 69, 1284–1305,
- 653 https://doi.org/10.1175/JAS-D-11-0225.1
- Dee, D. P., and Coauthors, 2011: The ERA-Interim reanalysis: Configuration and performance of
- 655 the data assimilation system. Quart. J. Roy. Meteor. Soc., 137, 553–597,
- 656 http://doi.org/10.1002/qj.828
- DeMaria, M., and J. Kaplan, 1999: An updated Statistical Hurricane Intensity Prediction Scheme
- (SHIPS) for the Atlantic and eastern North Pacific basins. Wea. Forecasting, 14, 326–337,
- https://doi.org/10.1175/1520-0434(1999)014<0326:AUSHIP>2.0.CO;2
- Elsberry, R. L., T. D. B. Lambert, and M. A. Boothe, 2007: Accuracy of Atlantic and eastern North
- Pacific tropical cyclone intensity forecast guidance. Wea. Forecasting, 22, 747–762,
- https://doi.org/10.1175/waf1015.1

- 663 Emanuel, K. A., 1986: An air-sea interaction theory of tropical cyclones. Part I: Steady-state
- 664 maintenance. J. Atmos. Sci., 43, 585–604, https://doi.org/10.1175/1520-
- 665 0469(1986)043<0585:AASITF>2.0.CO;2
- 666 Emanuel, K. A., 1988: The maximum intensity of hurricanes. J. Atmos. Sci., 45, 1143–1155,
- https://doi.org/10.1175/1520-0469(1988)045<1143:TMIOH>2.0.CO;2
- 668 Emanuel, K. A., 1995: Sensitivity of tropical cyclones to surface exchange coefficients and a
- revised steady-state model incorporating eye dynamics. J. Atmos. Sci., 52, 3969–3976,
- 670 https://doi.org/10.1175/1520-0469(1995)052<3969:SOTCTS>2.0.CO;2
- Emanuel, K. A., 1997: Some aspects of hurricane inner-core dynamics and energetics. *J. Atmos.*
- 672 *Sci.*, **54**, 1014–1026, https://doi.org/10.1175/1520-0469(1997)054<1014:SAOHIC>2.0.CO;2.
- Emanuel, K., 2000: A statistical analysis of tropical cyclone intensity. *Mon. Wea. Rev.*, **128**, 1139–
- 674 1152, https://doi.org/10.1175/1520-0493(2000)128<1139:ASAOTC>2.0.CO;2
- 675 Emanuel, K., C. DesAutels, C. Holloway, and R. Korty, 2004: Environmental control of tropical
- 676 cyclone intensity. *J. Atmos. Sci.*, **61**, 843–858, https://doi.org/10.1175/1520-
- 677 0469(2004)061<0843:ECOTCI>2.0.CO;2
- 678 Fowler, J. P., and T. J. Galarneau, 2017: Influence of storm-storm and storm-environment
- interactions on tropical cyclone formation and evolution. Mon. Wea. Rev., 145, 4855–4875,
- 680 https://doi.org/10.1175/MWR-D-17-0131.1
- Frank, W. M., and E. A. Ritchie, 2001: Effects of vertical wind shear on the intensity and structure
- of numerically simulated hurricanes. Mon. Wea. Rev., 129, 2249–2269,
- 683 https://doi.org/10.1175/1520-0493(2001)129<2249:EOVWSO>2.0.CO;2
- Friedman, J. H., 2001: Greedy function approximation: a gradient boosting machine. Ann. Stat.,
- **29**, 1189–1232, https://doi.org/10.1214/aos/1013203451
- Fu, H., and Y. Wang, 2017: Effect of uncertainties in sea surface temperature dataset on the
- simulation of typhoon Nangka (2015). Atmos. Sci. Lett., 19, e797,
- 688 https://doi.org/10.1002/asl.797
- 689 Fu, H., Y. Wang, M. Riemer, and Q. Li, 2019: Effect of unidirectional vertical wind shear on
- tropical cyclone intensity change Lower-layer shear versus upper-layer shear. J. Geophys. Res.,

- 691 **124**, 6265–6282, https://doi.org/10.1029/2019JD030586
- 692 Ge, X., D. Shi, and L. Guan, 2018: Monthly variations of tropical cyclone rapid intensification
- ratio in the western North Pacific. Atmos. Sci. Lett., 19, e814, https://doi.org/10.1002/asl.814.
- 694 Goldstein, A., A. Kapelner, J. Bleich, and E. Pitkin, 2015: Peeking inside the black box: Visualizing
- statistical learning with plots of individual conditional expectation. J. Comput. Graph. Stat., 24,
- 696 44–65, https://doi.org/10.1080/10618600.2014.907095
- 697 Gray, W. M., 1968: Global view of the origin of tropical disturbances and storms. *Mon. Wea. Rev.*,
- 698 **96**, 669–700, https://doi.org/10.1175/1520-0493(1968)096<0669:GVOTOO>2.0.CO;2.
- Hastie T., R. Tibshirani, and J. Friedman, 2009: The Elements of Statistical Learning, Second
- 700 Edition. Springer.
- Hendricks, E. A., M. S. Peng, B. Fu, and T. Li, 2010: Quantifying environmental control on tropical
- 702 cyclone intensity change. Mon. Wea. Rev., 138, 3243–3271,
- 703 https://doi.org/10.1175/2010MWR3185.1
- Holland, G. J., 1997: The maximum potential intensity of tropical cyclones. J. Atmos. Sci., 54,
- 705 2519–2541, https://doi.org/10.1175/1520-0469(1997)054<2519:TMPIOT>2.0.CO;2
- Houze, R. A., S. S. Chen, B. F. Smull, W.-C. Lee, and M. M. Bell, 2007: Hurricane intensity and
- eyewall replacement. *Science*, **315**, 1235–1239, https://doi.org/10.1126/science.1135650
- 708 Liang, J., L. Wu, and G. Gu, 2018: Rapid weakening of tropical cyclones in monsoon gyres over
- the tropical western North Pacific. J. Climate, 31, 1015–1028, https://doi.org/10.1175/jcli-d-16-
- 710 0784.1
- Jiang, H., J. P. Zagrodnik, C. Tao, and E. J. Zipser, 2018: Classifying precipitation types in tropical
- cyclones using the NRL 37 GHz color product. J. Geophys. Res., 123, 5509-5524,
- 713 https://doi.org/10.1029/2018JD028324
- Jin, Q., X. Fan, J. Liu, Z. Xue, and H. Jian, 2019: Using eXtreme Gradient BOOSTing to predict
- changes in tropical cyclone intensity over the western North Pacific. Atmosphere, 10, 341,
- 716 https://doi:10.3390/atmos10060341
- Juračić, A., and D. J. Raymond, 2016: The effects of moist entropy and moisture budgets on
- 718 tropical cyclone development. J. Geophys. Res., 121, 9458–9473,

- 719 https://doi.org/10.1002/2016jd025065
- 720 Kaplan, J., and M. DeMaria, 2003: Large-scale characteristics of rapidly intensifying tropical
- 721 cyclones in the North Atlantic basin. Wea. Forecasting, 18, 1093–1108,
- 722 https://doi.org/10.1175/1520-0434(2003)018<1093:LCORIT>2.0.CO;2
- Kaplan, J., M. DeMaria, and J. A. Knaff, 2010: A revised tropical cyclone rapid intensification
- index for the Atlantic and eastern North Pacific basins. Wea. Forecasting, 25, 220-241,
- 725 https://doi.org/10.1175/2009WAF2222280.1
- Knaff, J. A., S. A. Seseske, M. DeMaria, and J. L. Demuth, 2004: On the influences of vertical
- wind shear on symmetric tropical cyclone structure derived from AMSU. Mon. Wea. Rev., 132,
- 728 2503–2510, https://doi.org/10.1175/1520-0493(2004)132<2503:OTIOVW>2.0.CO;2
- Knaff, J. A., C. R. Sampson, and K. D. Musgrave, 2018: An operational rapid intensification
- 730 prediction aid for the western North Pacific. Wea. Forecasting, 33, 799–811,
- 731 https://doi.org/10.1175/WAF-D-18-0012.1
- Knapp, K. R., M. C. Kruk, D. H. Levinson, H. J. Diamond, and C. J. Neumann, 2010: The
- 733 International Best Track Archive for Climate Stewardship (IBTrACS): Unifying tropical
- 734 cyclone best track data. Bull. Amer. Meteor. Soc. 91, 363-376.
- 735 https://doi.org/10.1175/2009BAMS2755.1
- Knapp, K. R., H. J. Diamond, J. P. Kossin, M. C. Kruk, and C. J. Schreck, 2018: International Best
- 737 Track Archive for Climate Stewardship (IBTrACS) Project, Version 4. NOAA National Centers
- for Environmental Information. https://doi.org/10.25921/82ty-9e16
- Kurihara, Y., M. A. Bender, and R. J. Ross, 1993: An initialization scheme of hurricane models by
- vortex specification. Mon. Wea. Rev., 121, 2030-2045, https://doi.org/10.1175/1520-
- 741 0493(1993)121<2030:AISOHM>2.0.CO;2
- Kossin, J. P., and M. Sitkowski, 2012: Predicting hurricane intensity and structure changes
- associated with eyewall replacement cycles. Wea. Forecasting, 27, 484–488,
- 744 https://doi.org/10.1175/WAF-D-11-00106.1
- Kossin, J. P., 2015: Hurricane wind–pressure relationship and eyewall replacement cycles. Wea.
- 746 Forecasting, **30**, 177–181, https://doi.org/10.1175/WAF-D-14-00121.1.

- Kossin, J. P., and M. DeMaria, 2016: Reducing operational hurricane intensity forecast errors
- 748 during eyewall replacement cycles. Wea. Forecasting, 31, 601–608,
- 749 https://doi.org/10.1175/WAF-D-15-0123.1.
- 750 Lee, C.-Y., M. K. Tippett, S. J. Camargo, and A. H. Sobel, 2015: Probabilistic multiple linear
- regression modeling for tropical cyclone intensity. Mon. Wea Rev., 143, 933-954,
- 752 https://doi.org/10.1175/MWR-D-14-00171.1
- Ma, Z., J. Fei, and X. Huang, 2019: A definition of rapid weakening for tropical cyclones over the
- 754 western North Pacific. Geophys. Res. Lett., 46, 11471-11478,
- 755 https://doi.org/10.1029/2019GL085090
- 756 Miller, B. I., 1958: On the maximum intensity of hurricanes. J. Meteor., 15, 184–195,
- 757 https://doi.org/10.1175/1520-0469(1958)015<0184:OTMIOH>2.0.CO;2
- Montgomery, M. T., M. M. Bell, S. D. Aberson, and M. L. Black, 2006: Hurricane Isabel (2003):
- New insights into the physics of intense storms. Part I: Mean vortex structure and maximum
- intensity estimates. Bull. Amer. Meteor. Soc., 87, 1335–1347, https://doi.org/10.1175/BAMS-
- 761 87-10-1335
- Na, W., J. L. McBride, X.-H. Zhang, and Y.-H. Duan, 2018: Understanding biases in tropical
- cyclone intensity forecast error. Wea. Forecasting, 33, 129–138, https://doi.org/10.1175/WAF-
- 764 D-17-0106.1
- Peng, M. S., B.-F. Jeng, and R. T. Williams, 1999: A numerical study on tropical cyclone
- intensification. Part I: Beta effect and mean flow effect. J. Atmos. Sci., 56, 1404–1423,
- 767 https://doi.org/10.1175/1520-0469(1999)056<1404:ANSOTC>2.0.CO;2
- Persing, J., and M. T. Montgomery, 2003: Hurricane superintensity. J. Atmos. Sci., 60, 2349-2371,
- 769 https://doi.org/10.1175/1520-0469(2003)060<2349:HS>2.0.CO;2
- Riemer, M., and M. T. Montgomery, and M. E. Nicholls, 2010: A new paradigm for intensity
- modification of tropical cyclones: Thermodynamic impact of vertical wind shear on the inflow
- layer. Atmos. Chem. Phys., **10**, 3163–3188, https://doi.org/10.5194/acp-10-3163-2010
- Riemer, M., M. T. Montgomery, and M. E. Nicholls, 2013: Further examination of the
- thermodynamic modification of the inflow layer of tropical cyclones by vertical wind shear.

- 775 Atmos. Chem. Phys., 13, 327–346, https://doi.org/10.5194/acp-13-327-2013
- Rios-Berrios, R., and R. D. Torn, 2017: Climatological analysis of tropical cyclone intensity
- changes under moderate vertical wind shear. Mon. Wea. Rev., 145, 1717-1738,
- 778 https://doi.org/10.1175/MWR-D-16-0350.1
- Shu, S., and L. Wu, 2009: Analysis of the influence of Saharan air layer on tropical cyclone
- 780 intensity using AIRS/Aqua data. Geophys. Res. Lett., 36, L09809,
- 781 https://doi.org/10.1029/2009GL037634
- 782 Sikowski, M. J. P. Kossin, and C. M. Rozoff, 2011: Intensity and structure changes during
- hurricane eyewall replacement cycles. Mon. Wea. Rev., 139, 3829–3847,
- 784 https://doi.org/10.1175/MWR-D-11-00034.1
- 785 Tao, C., H. Jiang, and J. Zawislak, 2017: The relative importance of stratiform and convective
- rainfall in rapidly intensifying tropical cyclones, Mon. Wea. Rev., 145, 795-809,
- 787 https://doi.org/10.1175/MWR-D-16-0316.1
- Tang, B., and K. Emanuel, 2010: Midlevel ventilation's constraint on tropical cyclone intensity. *J.*
- 789 Atmos. Sci., **67**, 1817–1830, https://doi.org/10.1175/2010JAS3318.1
- 790 Tang, B., and K. Emanuel, 2012: Sensitivity of tropical cyclone intensity to ventilation in an
- 791 axisymmetric model. J. Atmos. Sci., **69**, 2394–2413, https://doi.org/10.1175/jas-d-11-0232.1.
- Walker, N. D., R. R. Leben, C. T. Pilley, M. Shannon, D. C. Herndon, I.-F. Pun, I.-I. Lin, and C.
- 793 L. Gentemann, 2014: Slow translational speed causes rapid collapse of northeast Pacific
- Hurricane Kenneth over cold core eddy. Geophys. Res. Lett., 41, 7595–7601,
- 795 https://doi.org/10.1002/2014GL061584
- Wang, Y., 2009: How do outer spiral rainbands affect tropical cyclone structure and intensity? J.
- 797 Atmos. Sci., 66, 1250-1273, https://doi.org/10.1175/2008JAS2737.1
- Wang, Y., Y. Rao, Z.-M. Tan, and D. Schönemann, 2015: A statistical analysis of the effects of
- vertical wind shear on tropical cyclone intensity change over the western North Pacific. *Mon.*
- 800 Wea. Rev., 143, 3434–3453, https://doi.org/10.1175/MWR-D-15-0049.1
- Willoughby, H. E., J. A. Clos, and M. G. Shoreibah, 1982: Concentric eye walls, secondary wind
- maxima, and the evolution of the hurricane vortex. J. Atmos. Sci., 39, 395–411,

- 803 https://doi.org/10.1175/1520-0469(1982)039<0395:CEWSWM>2.0.CO;2
- Wood, K. M., and E. A. Ritchie, 2015: A definition for rapid weakening of North Atlantic and
- eastern North Pacific tropical cyclones. Geophys. Res. Lett., 42, 10,091–10,097,
- 806 https://doi.org/10.1002/2015GL066697
- 807 Wu, L., and Coauthors, 2012: Relationship of environmental relative humidity with North Atlantic
- tropical cyclone intensity and intensification rate. Geophys. Res. Lett., 39, L20809,
- 809 https://doi.org/10.1029/2012GL053546
- 810 Xu, Y., and Y. Wang, 2013: On the initial development of asymmetric vertical motion and
- horizontal relative flow in a mature tropical cyclone embedded in environmental vertical shear.
- 812 *J. Atmos. Sci.*, **70**, 3471–3491, https://doi.org/10.1175/JAS-D-12-0335.1
- Yang, Y.-T., H.-C. Kuo, E. A. Hendricks, and M. S. Peng, 2013: Structural and intensity changes
- of concentric eyewall typhoons in the western North Pacific. Mon. Wea. Rev., 141, 2632–2648,
- 815 https://doi.org/10.1175/MWR-D-12-00251.1
- 816 Zeng, Z., Y. Wang, and C.-C. Wu, 2007: Environmental dynamical control of tropical cyclone
- 817 intensity-An observational study. Mon. Wea. Rev., 135, 38–59,
- 818 https://doi.org/10.1175/MWR3278.1
- 819 Zeng, Z., L. Chen, and Y. Wang, 2008: An observational study of environmental dynamical control
- of tropical cyclone intensity in the Atlantic. Mon. Wea. Rev., 136, 3307–3322,
- 821 https://doi.org/10.1175/2008MWR2388.1
- 822 Zeng, Z., Y. Wang, and L. Chen, 2010: A statistical analysis of vertical shear effect on tropical
- 823 cyclone intensity change in the North Atlantic. Geophys. Res. Lett. 37, L02802,
- https://doi.org/10.1029/2009GL041788

TABLE 1. The factors analyzed in this study with their units and descriptions.

Variables	Unit	Description
Vmax	m s ⁻¹	Initial TC intensity, calculated by subtracting 40% of SPD from the maximum wind speed in the best-track data
SST	$^{\circ}\mathrm{C}$	Initial sea surface temperature averaged within a radius of 300 km from the TC center
POT		Relative intensity, calculated as initial intensity divided by the corresponding MPI
DSST	$^{\circ}$ C	SST change within 24 hours along TC track
SPD	m s ⁻¹	Translational speed of the TC center
USPD	m s ⁻¹	Zonal translational speed of the TC center
VSPD	m s ⁻¹	Meridional translational speed of the TC center
VWS	m s ⁻¹	Area-averaged (200-800 km) 200-850-hPa vertical wind shear
DIV200	s^{-1}	Divergence averaged within a radius of 1000km from the TC center at 200 hPa
RHUL	%	Area (between 200 and 800 km radii)- and vertically (300-850 hPa)-averaged relative humidity in the upshear-left quadrant
RHUR	%	Similar to RHUL but in the upshear-right quadrant
RHDL	%	Similar to RHUL but in the downshear-left quadrant
RHDR	%	Similar to RHUL but in the downshear-right quadrant

TABLE 2. Statistics of RW and SW TCs for all and each interval of weakening duration (h) during 1980–2017: number of TCs (Num.), averages of weakening duration (Avg. weakening duration; h), RW duration (Avg. RW duration; h), proportion of RW duration to weakening duration (Avg. proportion; %) and lifetime maximum intensity (Avg. LMI; m s⁻¹).

	RW TCs					SW TCs		
weakening duration	Num.	Avg. weakening duration	Avg. RW duration	Avg. proportion	Avg. LMI	Num.	Avg. weakening duration	Avg. LMI
[24-48)	33	34	28	0.83	54.1	138	30	35.8
[48,72)	39	57	37	0.66	56.8	80	56	36.8
[72,96)	29	81	42	0.52	66.0	47	81	38.6
[96-120)	20	106	40	0.38	65.8	25	102	53.7
[120-144)	18	130	39	0.30	63.1	13	130	50.9
[144-168)	6	155	40	0.26	69.9	8	150	67.3
[168-192)	5	176	41	0.23	65.8	9	180	56.1
[192-216)	3	196	40	0.20	68.9	2	210	58.1
All	153	82	37	0.55	60.9	322	62	39.9

TABLE 3. List of correlation coefficients between TC WR and various parameters. The p values denote the statistical confidence of the corresponding correlation coefficient. Considering the case-size dependency [p value (C)] with 6 hourly data, p values based on the degree of freedom with TC number are shown as p value (T). Correlation coefficients that are statistically significant above 99% confidence level for p value (T) are bolded.

Parameters	Correlation coef.	p value (C)	p value (T)
Vmax	0.37	0	0
SST	-0.16	5.2×10^{-14}	4.5×10^{-4}
POT	0.40	0	0
DSST	-0.26	0	8.3×10^{-9}
SPD	0.22	0	1.2×10^{-6}
USPD	0.29	0	1.1×10^{-10}
VSPD	0.26	0	8.3×10^{-9}
VWS	0.29	0	1.1×10^{-10}
DIV200	0.07	9.4×10^{-5}	0.13
RHUL	-0.26	0	8.3×10^{-9}
RHUR	-0.08	8.0×10^{-6}	0.08
RHDL	-0.02	0.26	0.66
RHDR	-0.07	9.4×10^{-5}	0.13

LIST OF FIGURES

- Fig. 1. (a) Spatial distributions of TC WR (shaded, m s⁻¹ day⁻¹) and weakening case frequency (contour) in each 2.5°×2.5° grid box in typhoon seasons (from June to November) during 1980—2017. (b) Tracks of RW TCs in their lifetimes, note that the non-weakening stages are shown as white curves and the RW (SW) stages of RW TCs are marked as black (grey) curves, with the underlying shade denotes climatologically mean SST in typhoon seasons. (c) Same as (b) but for SW TCs.
- Fig. 2. Monthly variations of (a) all weakening TCs (grey) and RW TCs (black), and the ratio of RW TCs to total weakening TCs (curve), and (b) all weakening cases (grey) and RW cases (black), and the ratio of RW cases to total weakening cases (curve) from June to November during 1980 2017. The corresponding numbers are also given at the tops of their corresponding bars.
- Fig. 3. Scatter diagrams of TC WR against (a) Vmax, (b) SST, (c) POT (relative intensity; Vmax/MPI), (d) DSST, (e) USPD, and (f) VSPD. The fitted 95th, 75th and 50th percentiles of WRs are shown as black, green and red curves, respectively, and the curves are obtained using smoothed cubic spline approximation.
 - **Fig. 4.** The frequency distributions (right ordinate) of SW (grey bar) and RW (black bar) cases and corresponding cumulative probability density (left ordinate, blue and red curves) against (a) Vmax, (b) SST, (c) POT, (d) DSST, and (e) translational speed (SPD). (f) The frequency distribution of SW (blue) and RW (red) cases against translational speed zonal (USPD; solid) and meridional (VSPD; dashed) components, respectively.
 - **Fig. 5.** The vertical distributions of environmental U winds (m s⁻¹) as a function of POT for (a) SW, and (b) RW cases and those of environmental V winds (m s⁻¹) for SW and RW cases are shown in (d) and (e). The differences in environmental U and V winds between SW and RW groups are shown in (c) and (f), respectively.
 - **Fig. 6.** Left panels: same as Fig. 3 but for (a) deep-layer VWS (200-850hPa), (c) relative humidity in the upshear-left quadrant (RHUL), and (e) divergence at 200 hPa (DIV200); and right

865	panels: same as Fig. 4 but for (b) VWS (200-850hPa), (d) RHUL, and (f) DIV200.
866	Fig. 7. Relative importance of environmental factors used in the XGBoost model. Factors are listed
867	to the left in descending order of their relative importance. Description of these factors can be
868	found in Table 1
869	Fig. 8. The ICE plot of factors (a) POT, (b) DSST, (c) VWS and (d) RHUL, respectively. Thin
870	curves are XGBoost model-predicted WR as functions of one factor with all the other factors
871	fixed as observed from each individual sample. Thick curves are the 5th (black), 25th (red),
872	50th (green), and 75th (blue) percentiles of the predicted WRs, respectively.
873	Fig. 9. Same as Fig. 8 but for factors (a) USPD, (b) DIV200, and (c) VSPD, respectively.
874	

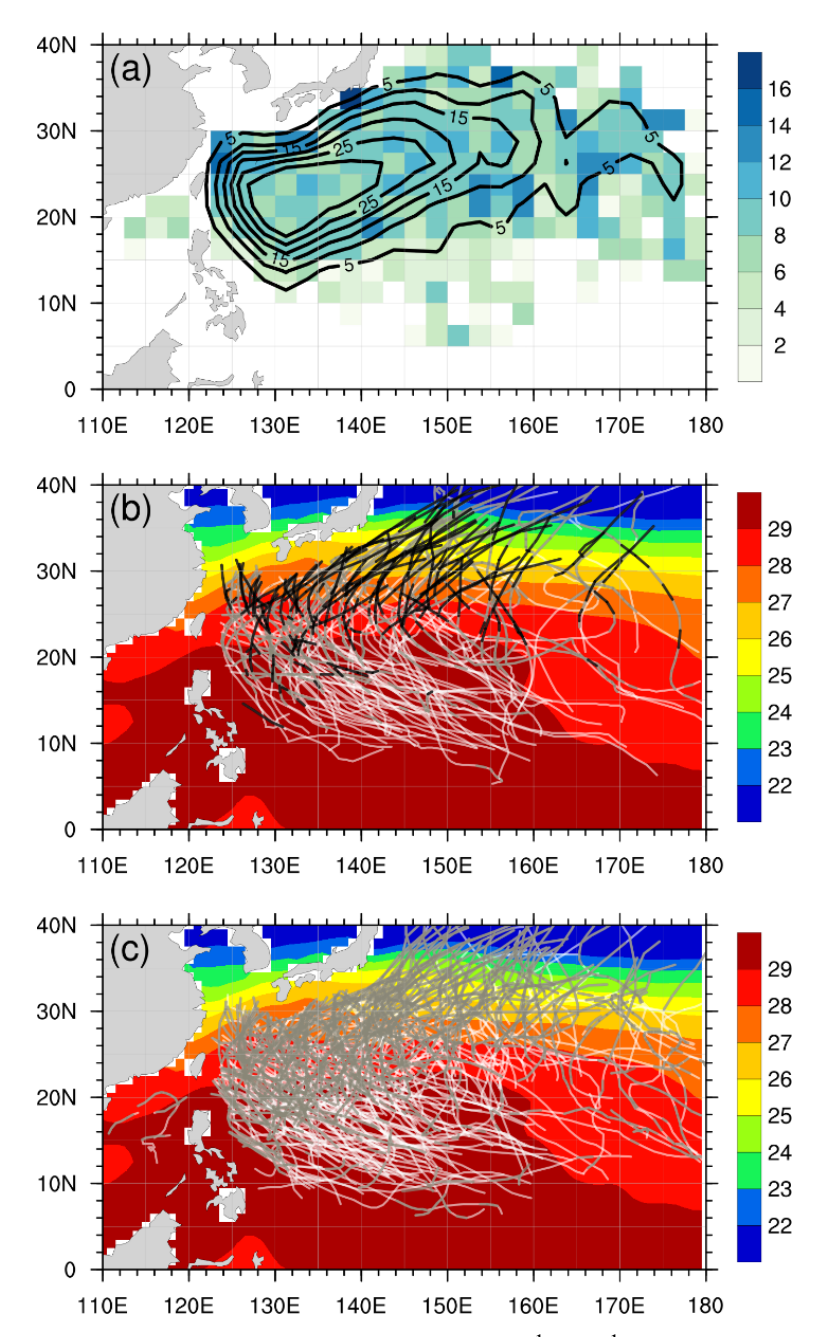


FIG. 1. (a) Spatial distributions of TC WR (shaded, m s⁻¹ day⁻¹) and weakening case frequency (contour) in each 2.5°×2.5° grid box in typhoon seasons (from June to November) during 1980—2017. (b) Tracks of RW TCs in their lifetimes, note that the weakening stages are shown as white curves and the RW (SW) stages of RW TCs are marked as black (grey) curves, with the underlying shade denotes climatologically mean SST in typhoon seasons. (c) Same as (b) but for SW TCs.

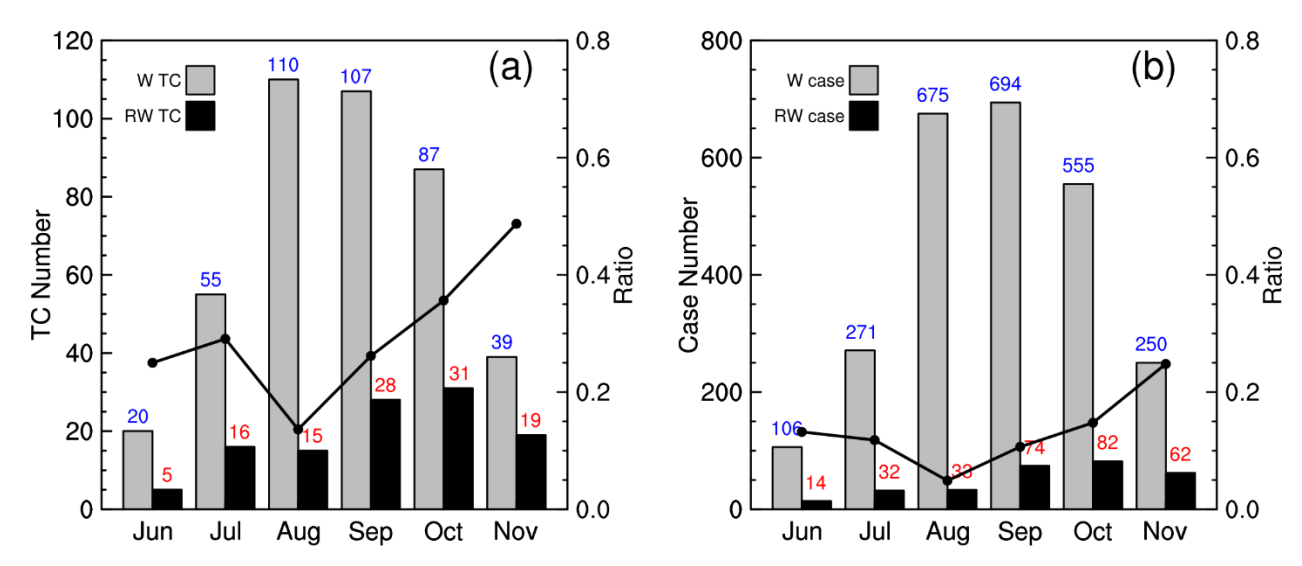


FIG. 2. Monthly variations of (a) all weakening TCs (grey) and RW TCs (black), and the ratio of RW TCs to total weakening TCs (curve), and (b) all weakening cases (grey) and RW cases (black), and the ratio of RW cases to total weakening cases (curve) from June to November during 1980–2017. The corresponding numbers are also given at the tops of their corresponding bars.

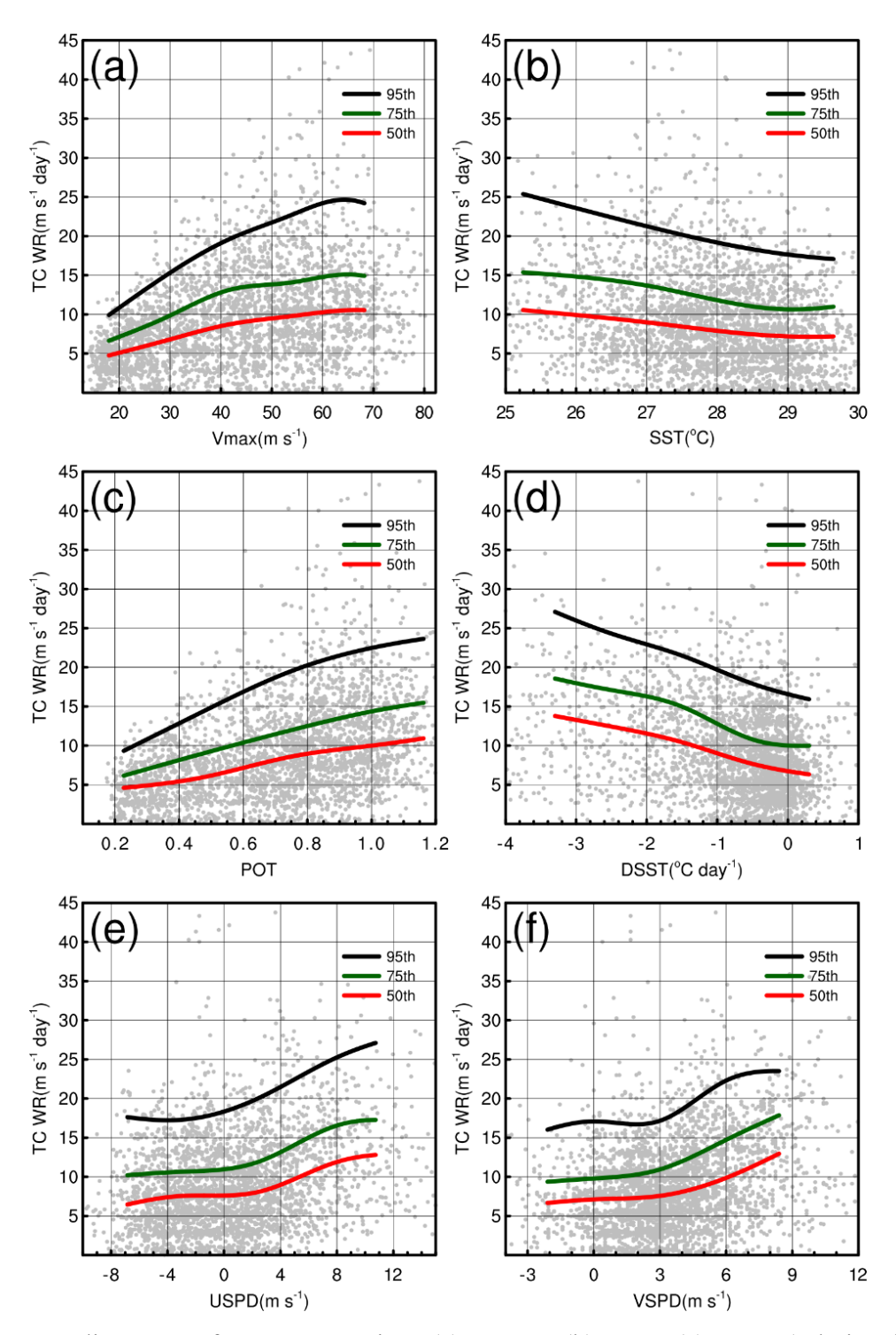


FIG. 3. Scatter diagrams of TC WR against (a) Vmax, (b) SST, (c) POT (relative intensity; Vmax/MPI), (d) DSST, (e) USPD, and (f) VSPD. The fitted 95th, 75th and 50th percentiles of WR are shown as black, green and red curves, respectively, and the curves are obtained using smoothed cubic spline approximation.

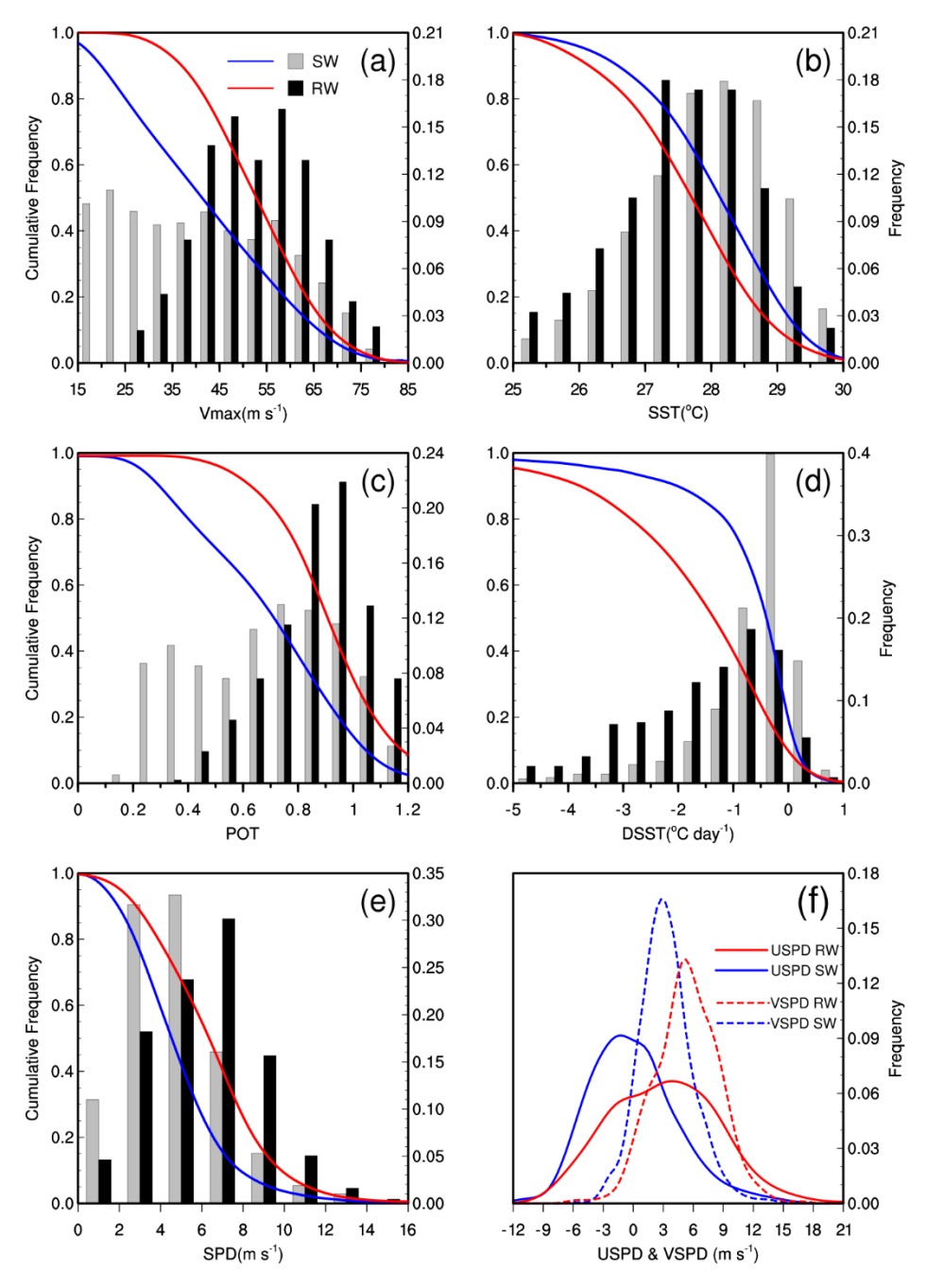


FIG. 4. The frequency distributions (right ordinate) of SW (grey bar) and RW (black bar) cases and corresponding cumulative probability density (left ordinate, blue and red curves) against (a) Vmax, (b) SST, (c) POT, (d) DSST, and (e) translational speed (SPD). (f) The frequency distribution of SW (blue) and RW (red) cases against translational speed zonal (USPD; solid) and meridional (VSPD; dashed) components, respectively.

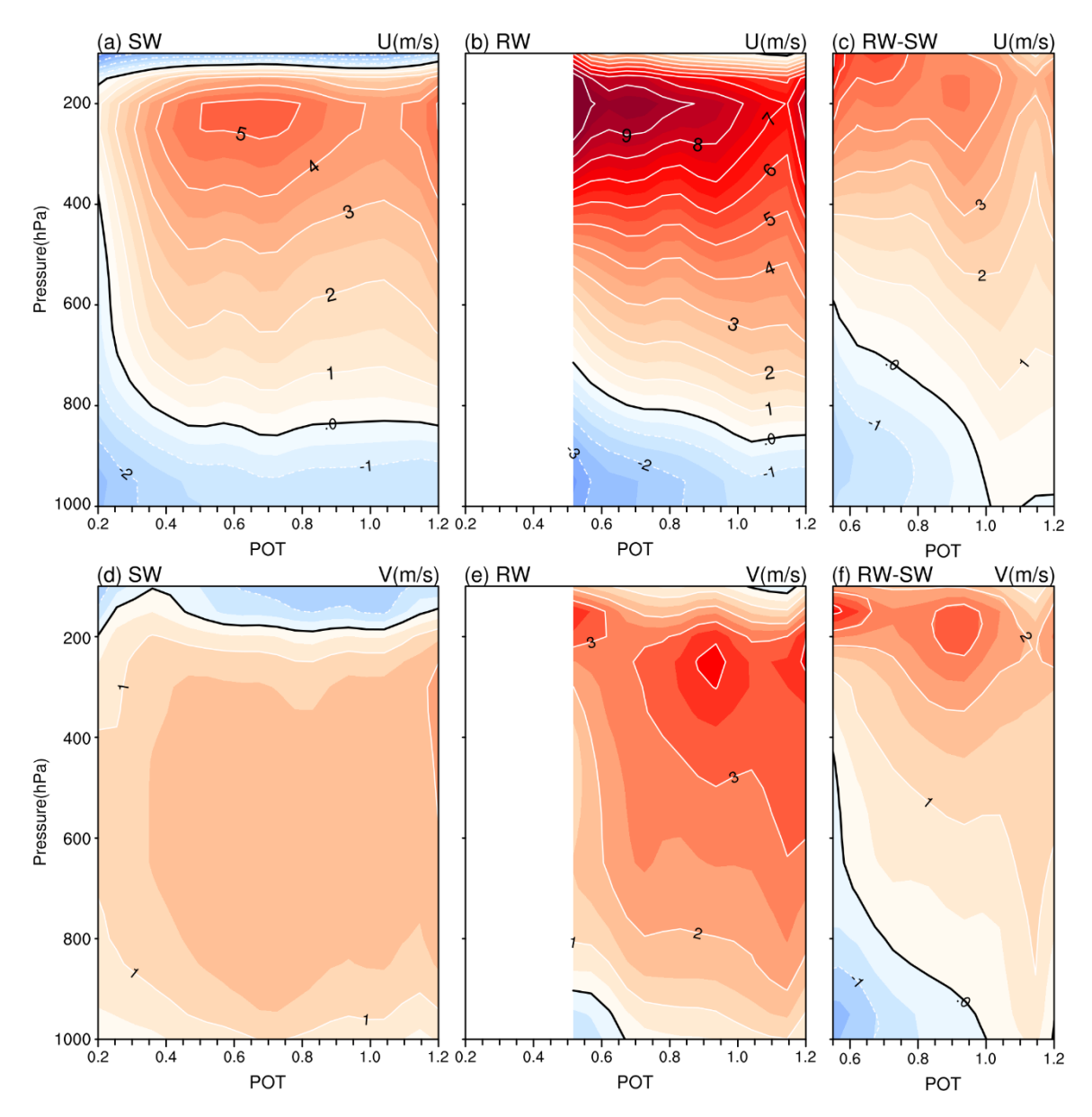


FIG. 5. The vertical distributions of environmental U winds (m s⁻¹) as a function of POTfor (a) SW, and (b) RW events and those of environmental V winds (m s⁻¹) for SW and RW events are shown in (d) and (e). The differences in environmental U and V winds between SW and RW groups are shown in (c) and (f), respectively.

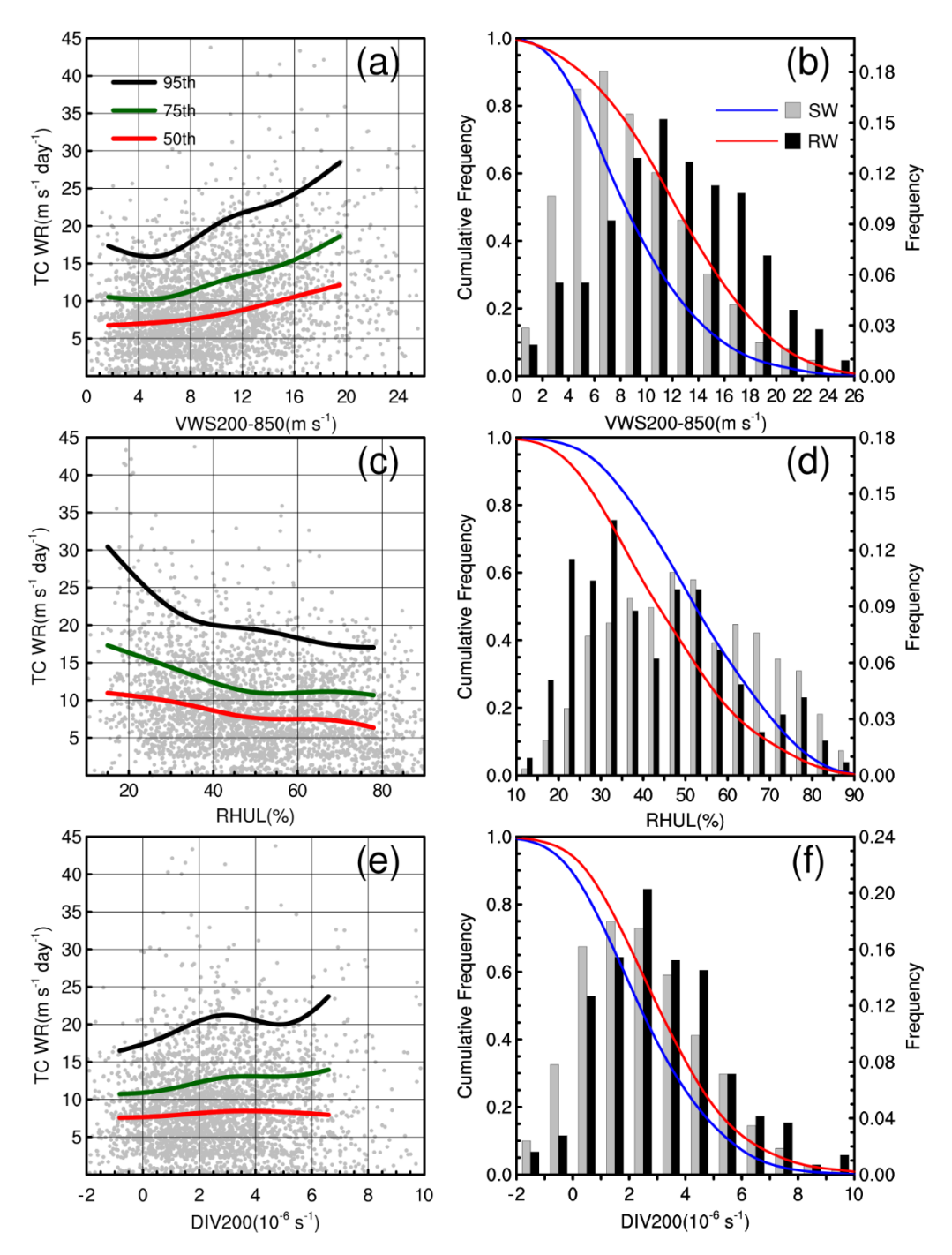


FIG. 6. Left panels: same as Fig. 3 but for (a) deep-layer VWS (200-850hPa), (c) relative humidity in the upshear-left quadrant (RHUL), and (e) divergence at 200 hPa (DIV200); and right panels: same as Fig. 4 but for (b) VWS (200-850hPa), (d) RHUL, and (f) DIV200.

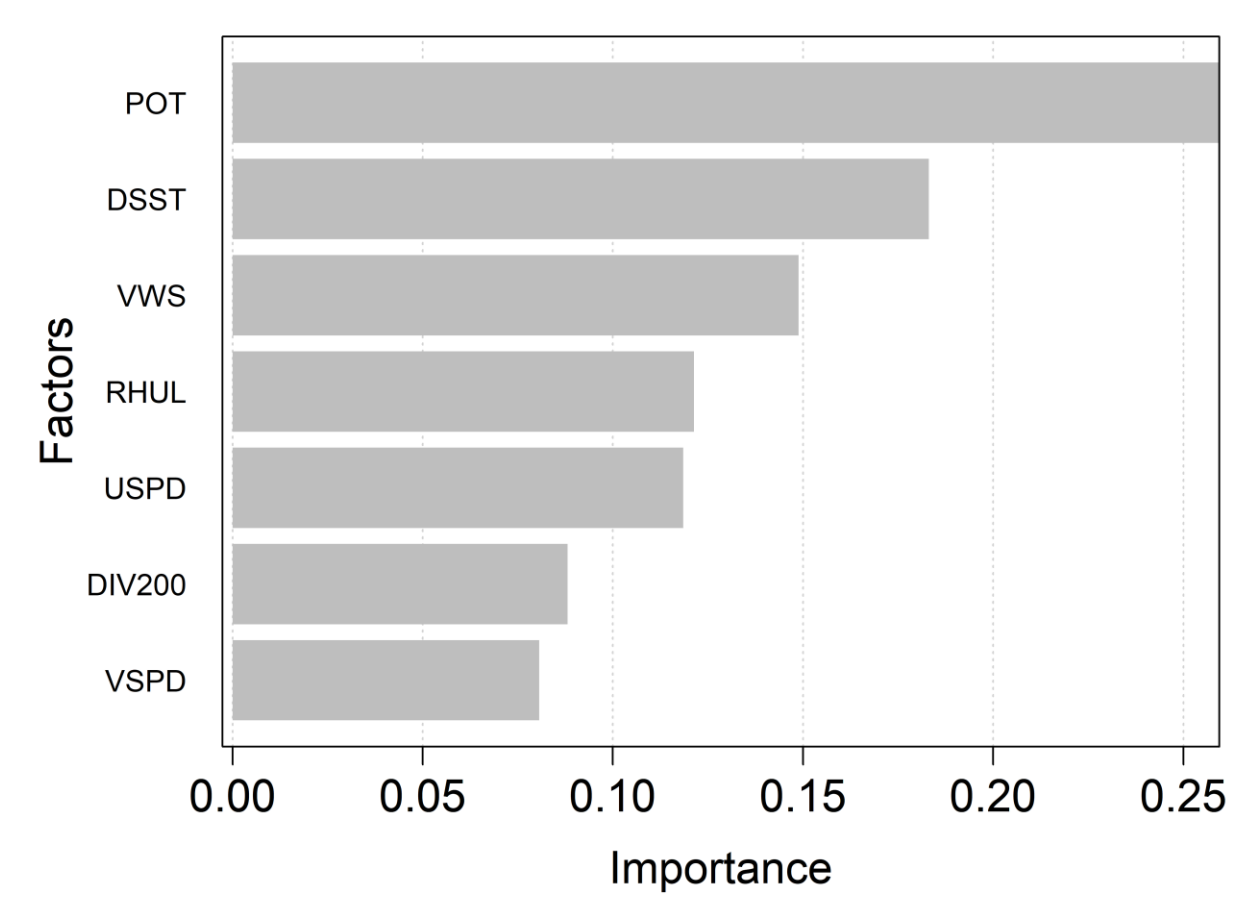


FIG. 7. Relative importance of environmental factors used in the XGBoost model. Factors are listed to the left in descending order of their relative importance. Description of these factors can be found in Table 1.

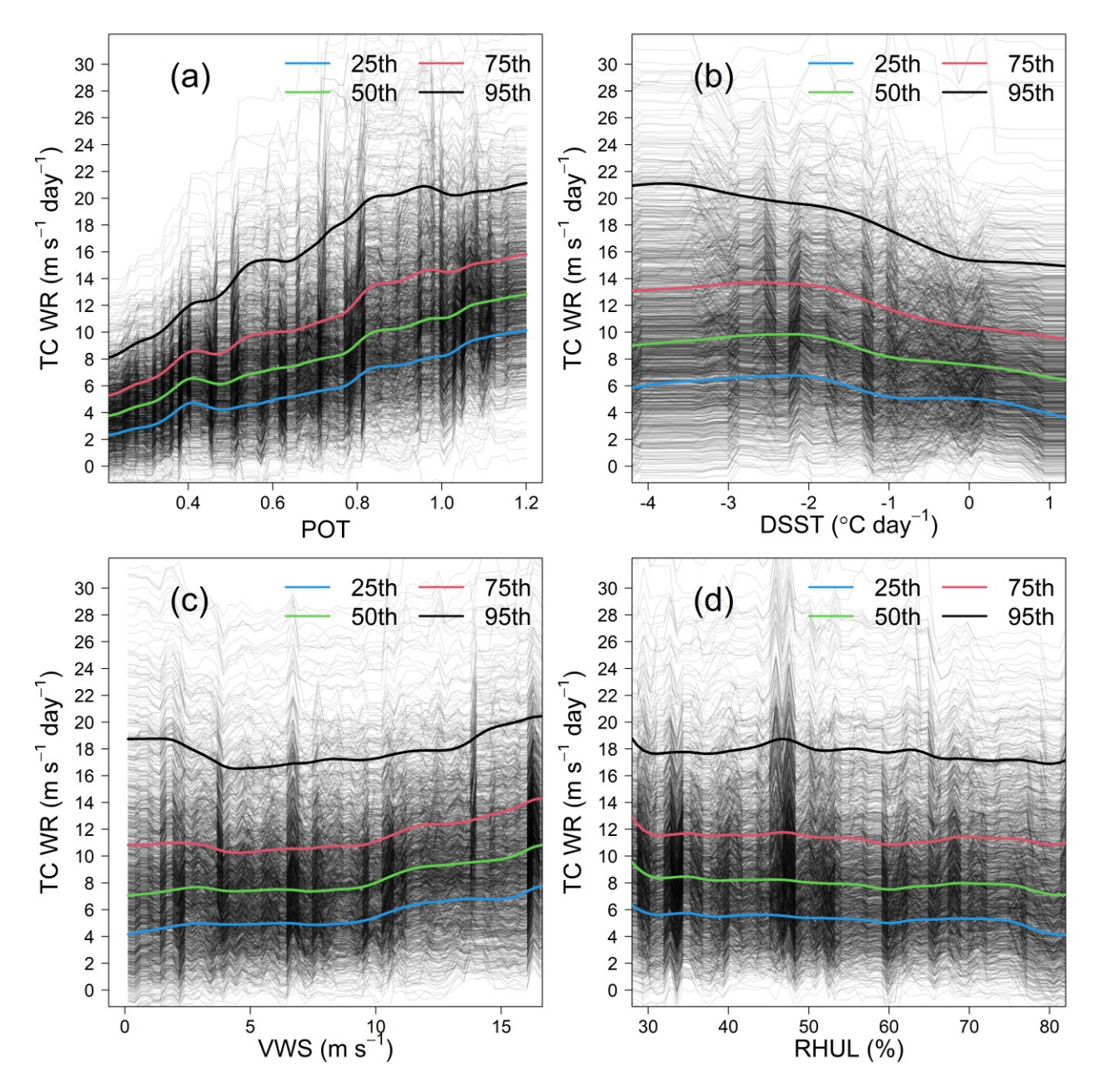
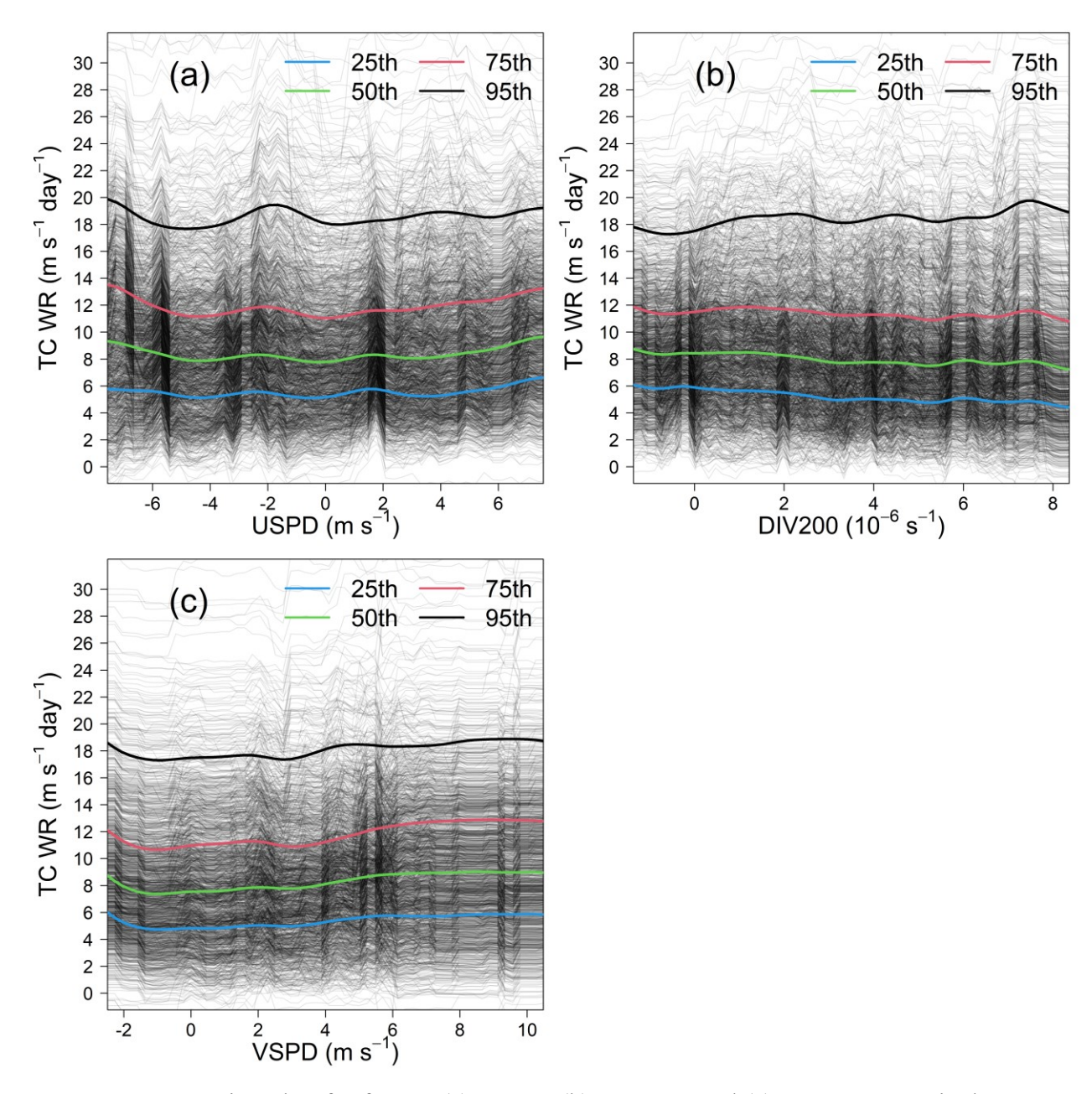


FIG. 8. The ICE plot of factors (a) POT, (b) DSST, (c) VWS and (d) RHUL, respectively. Thin curves are XGBoost model-predicted WR as functions of one factor with all the other factors fixed as observed from each individual sample. Thick curves are the 25th (blue), 50th (green), 75th (red), and 95th (black) percentiles of the predicted WR, respectively.



920 FIG. 9. Same as Fig. 8 but for factors (a) USPD, (b) DIV200, and (c) VSPD, respectively.